RESEARCH-ARTICLE

What is Affective Touch Made Of? A Soft Capacitive Sensor Array Reveals the Interplay between Shear, Normal Stress and Individuality

DEVYANI MCLAREN, The University of British Columbia, Vancouver, BC, Canada

JIAN GAO, The University of British Columbia, Vancouver, BC, Canada

XIULUN YIN, The University of British Columbia, Vancouver, BC, Canada

RÚBIA REIS GUERRA, The University of British Columbia, Vancouver, BC, Canada

PREETI VYAS, The University of British Columbia, Vancouver, BC, Canada

CHRYS MORTON, The University of British Columbia, Vancouver, BC, Canada

View all

Published: 11 October 2024

UIST '24: The 37th Annual ACM Symposium on User Interface Software and Technology
October 13 - 16, 2024
PA, Pittsburgh, USA

What is Affective Touch Made Of? A Soft Capacitive Sensor Array Reveals Interplay between Shear, Pressure and Individuality

Devyani McLaren*
Computer Science
University of British Columbia
Vancouver, BC, Canada
devyanim@cs.ubc.ca

Jian Gao*
Electrical & Computer Engineering
University of British Columbia
Vancouver, BC, Canada
gaojian1@student.ubc.ca

Xiulun Yin
Electrical & Computer Engineering
University of British Columbia
Vancouver, BC, Canada
huronyin@student.ubc.ca

Rúbia Reis Guerra
Computer Science
University of British Columbia
Vancouver, BC, Canada
rubiarg@cs.ubc.ca

Preeti Vyas
Computer Science
University of British Columbia
Vancouver, BC, Canada
pv@cs.ubc.ca

Chrys Morton
Biomedical Engineering
University of British Columbia
Vancouver, BC, Canada
morton9@student.ubc.ca

Xi Laura Cang
Computer Science
University of British Columbia
Vancouver, BC, Canada
cang@cs.ubc.ca

Yizhong Chen
Electrical & Computer Engineering
University of British Columbia
Vancouver, BC, Canada
librason@student.ubc.ca

Yiyuan Sun
Computer Science University of British Columbia
Vancouver, BC, Canada
sun1092@student.ubc.ca

Ying Li
Electrical & Computer Engineering
University of British Columbia
Vancouver, BC, Canada
jacintal@student.ubc.ca

John D. W. Madden
Electrical & Computer Engineering
University of British Columbia
Vancouver, BC, Canada
jmadden@ece.ubc.ca

Karon E. MacLean
Computer Science
University of British Columbia
Vancouver, BC, Canada
maclean@cs.ubc.ca

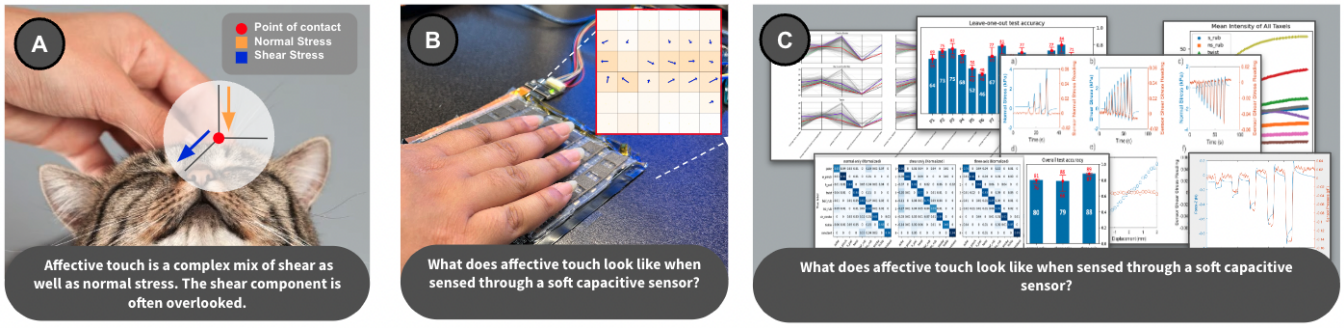

Figure 1: Tracing the role of shear in affective touch. (a) Humans affectively touch objects and creatures with complex forces. (b) We adapted a soft capacitive sensor to capture affective-touch levels of normal and shear stress (inset shows shear (blue arrows) and normal stress (orange heatmap) for *Back and Forth Rub*). (c) We found that shear is at least or more important than normal stress in affective touch gesture recognition. We analyzed specific gestures and individual differences to understand how features vary and their critical range.

*These authors contributed equally to this research.

UIST '24, October 13–16, 2024, Pittsburgh, PA, USA

ACM ISBN 979-8-4007-0628-8/24/10
https://doi.org/10.1145/3654777.3676346

ABSTRACT

Humans physically express emotion by modulating parameters that register on mammalian skin mechanoreceptors, but are unavailable in current touch-sensing technology. Greater sensory richness combined with data on affect-expression composition is a prerequisite to estimating affect from touch, with applications including physical human-robot interaction. To examine shear alongside more easily captured normal stresses, we tailored recent capacitive technology

to attain performance suitable for affective touch, creating a flexible, reconfigurable and soft 36-taxel array that detects multitouch normal and 2-dimensional shear at ranges of 1.5kPa-43kPa and ± 0.3-3.8kPa respectively, wirelessly at 43Hz (1548 taxels/s). In a deep-learning classification of 9 gestures (N=16), inclusion of shear data improved accuracy to 88%, compared to 80% with normal stress data alone, confirming shear stress's expressive centrality. Using this rich data, we analyse the interplay of sensed-touch features, gesture attributes and individual differences, propose affective-touch sensing requirements, and share technical considerations for performance and practicality.

CCS CONCEPTS

• **General and reference** → Design; • **Human-centered computing** → *Haptic devices*; • **Hardware** → *Haptic devices*; **Sensors and actuators**; • **Computing methodologies** → **Machine learning**.

KEYWORDS

Sensors; Touch Surfaces and Touch Interaction; Touch; Haptic; Gesture; Machine Learning; Affective Computing

ACM Reference Format:

Devyani McLaren, Jian Gao, Xiulun Yin, Rúbia Reis Guerra, Preeti Vyas, Chrys Morton, Xi Laura Cang, Yizhong Chen, Yiyuan Sun, Ying Li, John D. W. Madden, and Karon E. MacLean. 2024. What is Affective Touch Made Of? A Soft Capacitive Sensor Array Reveals Interplay between Shear, Pressure and Individuality. In *The 37th Annual ACM Symposium on User Interface Software and Technology (UIST '24), October 13–16, 2024, Pittsburgh, PA, USA.* ACM, New York, NY, USA, 31 pages. https://doi.org/10.1145/3654777.3676346

1 INTRODUCTION

What happens when you pet a cat? You might scrub her ears just where she likes it; she rolls over, you tickle her belly and wiggle her paws. You both are thinking *play, pleasure, what do I like, what does she like?* At another time, you realize *she's anxious*, so you stroke her slowly and softly to calm her. If *she missed me while I was gone*, you hold and gently squeeze her. Always, you continuously communicate through quickly evolving tactile exchanges, estimating and often trying to alter the others' emotional balance.

A robot able to interact in a physically nuanced way with a human partner would provide exceptional visibility into the physical and neurological mechanisms of affective touch [19, 56, 59]; and support personalized, unobtrusive guidance in therapeutic regulation of emotion and pain [5, 6, 32, 50].

Touch Sensing Requirements: Such a robot needs skin that combines materiality and tactile sensing capabilities near enough to that of humans and cats that we can discover the characteristics essential to modeling affective touch (Figure 1). Through its skin mechanoreceptors, viscoelastic and frictional properties and neural wiring [22, 39], mammalian skin is magnificently evolved for this purpose, able to sense, process and react to shear, pressure, localization, temperature and pain, simultaneously and rapidly.

It is empirically possible to distinguish many social-touch *gestures* using normal stress alone, with relatively low spatial resolution (*e.g.*, fingerpad-sized taxels [17, 21, 30, 52]). But since people use the same gestures for many emotion-communication purposes [97], on its own gesture gives inadequate insight into affective state.

The Case for Shear: Additional information seems to be embedded in *the way affective gestures are carried out*, and how gestural parameters *change over time* [8, 16, 18]. For now, we can only guess at what features matter; but we clearly need more than pressure and localization. Common movements like stretch, drag, pinch and scratch all engage skin shearing[1]. To capture the additional touch nuances that may indicate *emotion*, we need access to shear.

A Shear Challenge: Sensing direct-touch shear stresses across a surface is a complex proposition. Shear involves displacement and force applied tangentially to the surface. A vector quantity, it is related non-linearly to normal stress by friction, shifting modes among sliding, stick-slip and isometric shear for a given normal and tangential stress. Dragging on the skin is transmitted non-linearly to the sensor substructure, generating mechanical and electrical cross-talk with adjacent regions and with normal stress sensing. If a sensor has discrete taxels, then transverse sliding crosses boundaries and inter-taxel deadzones. A shear+normal stress sensor must be optimized in concert with modeling methods to minimize these considerations, using curated gestural data. The sensor's fabrication and wiring should enable non-rectilinear tailoring to cover arbitrary shapes, achieve speeds enabling realtime human-robot interaction, and be low enough in cost and effort for covering large surfaces to be feasible.

The opportunities for shear-sensitive skin span collecting and modeling affective touch in many contexts — wrapped on a handheld device, personal fidget object, or car steering wheel: wherever strong emotions will occur in conjunction with a touching opportunity and an intelligent system that could helpfully respond.

Progress: Multi-taxel robot skins have exhibited biomimicry in specific respects: flexible, stretchy, smooth, effective on soft surfaces, *or* able to sense multi-touch pressure and location [87]. The closest to managing it in a single package is Choi *et al* [21]'s 49-taxel sensor array, with millimeter-scale magnets embedded in 6mm-tall, 15mm-spaced pillars of silicone rubber on a flexible printed circuit board. Including shear information improved, deep-learning recognition accuracy for 13 gestures from 66% to 74%.

With this encouraging but black-box result, generating reliable requirements and enabling further technical evolution needs more transparency to determine *how* shear is involved in affective gesture, and how sensors should be built to optimize this.

1.1 Approach

To this end, we substantively and iteratively adapted an alternative technology (soft polymer capacitive arrays) with traits making it promising for capturing affective touch stresses: thin (<3mm), bendable at >10mm radius, smooth-surfaced and inclusion-free, tailorable in layout, and low-cost [35, 61, 75, 94]. Original versions lacked normal and shear sensitivity needed for affective gesture classification, and we further had to generate a spatially steady shear signal from discrete taxels. Our final design (§4) senses two-dimensional shear plus normal stress on $14{\times}14mm^2$ taxels, each with 5 channels, all sampled wirelessly at 43 Hz; we report its characterization for parameters likely to be important for affect applications (§5). To assess feature interplay and individual differences,

[1] Stress is force/unit area. A normal stress is applied orthogonally to the surface, while shear is applied transversely.

we modeled and analyzed data collected from a final, carefully diversified 9-gesture set that expands on those typically reported to include shear-intensive items, with 88% general accuracy (§6). Our current prototype is intended for placement on a robot or physically interactive surface to provide it with affective-touch perception, rather than as a pass-through sensor on a living, sensate body (a potential future application.

Iteration: Our approach was dominated by the absence of sensing requirements for estimating affective state. We required a sensor even to explore needed performance. Sensor design thus had to evolve alongside development of a data collection protocol and modelling pipeline, finally converging on a sensor structure and parameterization (resolution, precision, range) that aligns with how people form a range of affective touch gestures.

Rationale for Non-Authentic Gesture: We used performed affective-touch gestures to bootstrap development. Extensive iteration demanded efficient data collection; however, acquiring authentically emotive touch is a major undertaking [4, 18]. Although gesture *identity* is unlikely to provide affective state on its own, gestures carry this information in the nuances of how they are carried out. If performed with instructions to cover the expressive range that we expect to see in authentic emotive touch, they practically exercise sensor capability, while giving an indication of the most promising (*i.e.*, expressive) features for eventual emotion modeling in a more arduous authentic-emotion deployment.

Gestural Constraint: The challenge then becomes finding the right level of gestural constraint. Constraint detracts from realism and individual variation, but its absence impedes debugging a long pipeline: data collection, sensor design, fabrication, and training and comparing classification algorithms. Further, past work on social touch sensing relies almost exclusively on constrained performed gesture, to which we needed to compare our results.

We experimented with varying degrees of gesture constraint, and report on a moderate level that balances *data richness* (adequate activity across a set of informative features), *comparability* (has subsets that are comparable to past work), and *practicality* (our refined study protocol could be collected within about a week, allowing system iteration over a period of months).

1.2 Research Questions and Contributions

This project was framed around several research questions relating to this new technology and its suitability for capturing nuanced affective information via touch.

RQ1: What quality of affective touch gesture data is enabled by this **sensor technology**? *Contributes: Sensitivity and range, identification of features most sensitive to affective touch nuance, insights into best practices for design and fabrication.*

RQ2: How well can affective touch data from this technology be **modeled**? *Best-performing methods; model insight.*

RQ3: What does **shear add to normal stress and localization** data in gesture recognition performance? *Overall performance; gestural variation in shear/normal stress involvement.*

RQ4: What kinds and degree of **human individual differences** do we see in gesture performance, even with moderately constrained affective gestures? *Clear evidence of this technology's ability to capture nuance, and a need for individualized models.*

2 RELATED WORK

To ground the need and suitability of the novel sensor presented here, we discuss past affective touch applications to capture their specific requirements and technologies used (Tables 1-2), examine reported touch sensors and their technological approaches, then summarize computational methods which have been used to detect the types of gestures relevant to affective touch.

2.1 Affective Touch Applications

Affective haptic systems generally rely on some form of sensing to predict users' affective states in the course of touch-based interactions, and have been deployed in a number of application categories [5, 46]. In *emotion communication*, the touch sensor registers emotionally-salient input from an individual, relaying it to another (often non-co-located) individual [31, 47, 48, 99]. In *body awareness applications*, data extracted from tactile interaction with everyday objects [82] or wearables [77, 88] is used to enhance emotional state awareness. *Emotion regulation support* applications, often explored through touch-centric robot companions [13, 14, 17, 30, 83], may use haptic responsiveness to provide some manner of support.

Due to the limited capabilities of touch-sensing technologies and modeling methods, researchers of affective haptic applications often opt for sensors detecting basic touch parameters, *e.g.*, binary touch/not-touched state [31, 48, 89]; single-parametered touch (*e.g.*, location [47] *or* pressure [33, 90]); or two at once [15, 17, 30].

Because affective touch interactions often involve sliding, dragging, and stroking motions, researchers have articulated the need for touch sensors able to capture shear as well as normal stresses [10, 11, 27]. Shear stress sensors have appeared in electrical/electronic engineering [21, 68] and material science [40]. Choi *et al* [21] provided an initial demonstration that shear can increase the accuracy of gesture recognition over normal stress alone.

2.2 Related Sensor Technology

Flexible, soft stress sensors have potential application in advanced robotic sensory systems [25, 26], consumer electronics [58, 92], and human-computer interaction [49, 69, 79, 86], where researchers have explored piezoresistive [37, 70], capacitive [23, 54], piezoelectric [44, 53, 65] and magnetic [21, 62, 87] sensing technologies. This maturity is a boon for rapid prototyping as well as sensor deployment in consumer products. Moreover, when incorporating shear stress sensing capability, flexible capacitive sensors [29, 35, 41, 75] are favoured due to ease of electrode layout, compared with the preliminary piezoresistive systems [24, 57] available for normal and shear/three-axis stress measurement.

To achieve localization and increase sensing area, flexible sensors often employ arrays of *taxels*, adjusting inter-taxel distance for needed spatial resolution. Cang *et al* [17] used a 10×10 textile piezoresistive array able to capture normal stress between 0.005-1kg for a 100in^2 surface; Nguyen *et al* [64] demonstrated a 4×4 capacitive array (size not reported); with ionic liquid electrodes,

with taxels capturing both normal stress and proximity. Tomo *et al* [87] applied a magnetic-based, 4x4 'uSkin' array to a humanoid robotic hand, covering a 200mm^2 surface (force range not reported). An array's area may be limited by the minimum fabricable taxel size, tolerable width of unsensed inter-taxel gaps, and/or electronic multiplexing and data transmission considerations. Technology also dictates whether taxels can be arranged in an arbitrary pattern rather than a rectilinear grid to leverage its flexibility. Constraints on footprint shape and overall area are relevant in choosing an application's sensor technology.

In practical applications that engage wearables (out of scope for our technology) or robots (in scope) in human-environment or human-human interaction, contact often involves both tangential (sliding or isometric) as well as normal stress [78, 81]. Emerging evidence of the importance of shear in characterizing interactions has lead to interest in soft sensing devices able to discriminate three-axis stresses while maintaining a soft and skin-like surface feel [12, 73]. Two recent flexible sensing arrays capture both normal and shear stress. Cheng *et al* [20] proposed a flexible 8×8 capacitive shear sensing array (8mm^2 taxels), each with a bump made of PDMS (a form of silicone elastomer) atop electrodes embedded in a custom PDMS structure and a flexible printed circuit board (FPCB). Stresses applied to the bump are computed from capacitance changes in 4 channels. Meanwhile, Choi *et al* [21] developed a 5×9 magnetic shear array (15mm^2 taxels) with a similar stack layout. Force-driven displacement of a commercial hard disc magnet embedded in PDMS in each taxel was captured by a Hall effect sensor in a bottom layer.

Both approaches require physical bumps on each taxel; in the described validation studies, the bumps also served as a visual cue to confine users' input to the sensor areas with the best sensitivity. Both the surface bump and, at least in [21], the magnet inclusion, could be felt in stroking and palpating touch. This is unsuitable when the goal is to mimic natural, smooth skin free of inclusions, with relatively uniform sensitivity and unobstructed sliding contact. To meet our own deployment needs, we also required smaller readout circuits (compared to >64×64mm^2 and 61×18mm^2 as reported by [20] and [3, 21] respectively), lower power consumption (600, 330mW), and wireless data transmission for untethered operation.

Other approaches have developed sensors to bio-mimic skin sensing [66, 84]. Most relevant is SenSkin (Ogata *et al*, [67]), which measures skin deformation with a three-axis stress sensor composed of infrared (IR) reflective elements that capture tangential (perpendicular) and normal stress in wearable applications.

SenSkin measures shear indirectly through tangential stress detection. The infrared (IR) transmissions across a patch of skin are unable to pinpoint the exact location of touch within the patch or identify multiple touch points. Our sensor, however, is capable of detecting 2D finger motion and can observe tangential stress at a contact point as shear.

Detection of shear on our sensor is achieved through a layered-constructed taxels, which allows for detection of shear and normal stress, multiple contacts localized to taxel, and 2D finger motion more directly by converting the mechanical stimuli of touch into a change in capacitance.

2.3 Gesture Classification

Affective touch is challenging to model, with a large feature space (type of touch, location, duration, pressure, shear and combinations) and interpersonal variability. Hence, for early-stage understanding and designing relevant technologies, researchers have discretized the affective touch space by trying to recognize tactile gestures [97] that might convey or relate to specific affective states. They then used classification approaches to model and identify these gestures from touch input.

Modeling methods have included Bayesian classifiers [52], decisions trees [55], random forests [17], SVMs [51], simple neural networks [80] as well as deep-learning methods involving CNN [7, 21, 74] and RNNs [45]. Random forest classifiers have successfully demonstrated high accuracy rates upto 95% for discriminating 6 touch gestures [17], 94% for 9 [30], and 48% for 26 [9] and proven to be more effective as compared to naive Bayes, k-nearest, decision tree, and multilayer perception approaches [9]

More recent deep learning methods, particularly 3D convolutional neural networks (3DCNNs), have shown promise in gesture classification with touch data. Past work with this approach demonstrated a recognition accuracy of 74% [21], and 76.1% [98] using 3DCNNs for social touch gesture recognition, outperforming other methods for the same dataset. Similarly, there are reported improvements to accuracy in EMG-based hand gesture recognition with a parallel architecture of five convolution layers [95]. In this work, we choose to model our gesture data with 3DCNNs due to its ability to capture spatio-temporal information, which is crucial in touch data analysis. This is particularly important because we are introducing a new data channel – shear – for which effective handcrafted features for gesture classification have not yet been established. Since this is a benchmark with this sensor, we opted for using 3DCNNs to handle feature extraction automatically.

However, 3DCNNs have limitations. They require a large amount of training data [38], and produce inscrutable black-box models — we cannot easily explain how a 3DCNN arrives at its predictions. To address this issue, we have implemented a parallel analysis with handcrafted features for comparison to the 3DCNN. Future work could also involve analyzing the intermediate feature maps generated by the 3DCNN to gain insights into the features the model learns during the training process.

3 ESTIMATING REQUIREMENTS

We use descriptors of human touch (Table 1) as a bridge to establish technical requirements for a touch sensor able to detect and classify affective touch (Table 2) in order to support future refinement guided by realistic field use.

3.1 Describing Human Affective Touch

In a social context, affective touch can be described as a nuanced tactile exchange having emotional significance; in neuroscience, it is understood as a complex sensory phenomenon that involves the modulation of C-tactile afferent activity [60], integrating various touch contacts on the body, and engaging complex brain processes with emotional and social context. This dynamic, personalized, and context-sensitive exchange plays a pivotal role in human connection and emotional well-being, making it a captivating subject

Table 1: Morphological properties of manual affective touch gestures, from the perspective of the toucher. Ranges and estimates are for gestural components of affiliative affective touch, omitting aspects such as contacting surface temperature, materiality and shape.

	Gesture Property	Description	Relevance of Property to Affective Communication	Examples and estimated values
Spatial	Body location	Location on another body or object that is being touched	The recipient's skin varies in tactile sensitivity based on body location. From a social standpont, touching different body locations conveys social meaning, which can vary culturally.	Hand: greeting, soothing, comfort Shoulder: greeting, warmth, warning Leg: attention. [O]
	Contact area & hand extent	Size of area touched, and parts of hand used to make the touch	Large- vs small-contact gestures (e.g., full-hand vs. fingertip) differ in sensory involvement for both giver and receiver, and support other gestural variations (e.g., squeezing, encircling).	Small (5 sq. cm): attention-seeking Large (20 sq. cm): reassurance [O]
	Gesture travel	The gesture's largest displacement or movement length	Gestures often have "typical" extents, but this parameter might also be modulated to communicate mood, e.g., playfulness or intensity.	E.g., Poke (point-contact) to Hug (full enclosure of an object) [O]
Mechanical	Forcefulness	Magnitude of stress applied at a point of contact, in any direction	Gentle touch may convey tenderness or tentativeness; firm: support, urgency, dominance. Variation within a gesture or at different times can alter a gesture's meaning.	Light touches: 0.3N Heavy touches: 1.2N (Teyssier'2020, [S])
	Stress angle	Angle at which normal and shear stress are applied	Touch orientation (finger angle & linear/rotating movement direction) is a defining gesture property and provides context for the receiver to make sense of the communication.	E.g., circular or dragging versus stationary squeezing or poking
	Sliding contact	Degree to which gesture moves point of contact	A sliding touch (shear stress exceeds static friction) can cover more area, and must either be lighter or utlize a slicker surface than nonsliding, allowing different expressive parameters.	E.g., Stroke tends be lighter and longer, while a isometric Rub may be more fixed but deep; both engage shear.
	Stress modulation	Degree of change in applied normal and shear stress during the gesture	Touch that is steady vs. uses the full "natural" range of stress intensity can both define a gesture and change its meaning.	E.g, a modulated touch might be playful (tickle) in contrast to a steady, comforting one
Temporal	Duration	The length of time for a single contact (e.g., contact duration of a single tap in a series)	Temporal extent (brief vs. sustained) together with dynamics (what's happening over that contact) both defines the gesture, and can modulate both meaning or purpose.	E.g., a (short to long) static touch might invite play, attention, comfort. Tap (short): 0.05s (Asakawa'2017, [S]) Spontaneous embraces (long): 3s (Nagy'2011, [S])
	Velocity	The primary speed with which the touch is performed	Speed often conveys an intended emotion-regulatory direction: fast touch sends it upward, asking the other to play, or pay attention; while a slow touch sends it down, inviting calm.	1 to 16 cm/s (Morrison'2010, [S])
	Repetitiveness	The basic movement's tendency to be used once or multiply (regardless of breaking contact)	A single instance of touch might serve to alert, while repeated touches or a periodic pattern in a continuous touch may signify emphasis or persistence.	E.g., Hug: once; Poke/Pat: several [O]
	Repetition frequency	The rate at which a touch is repeated	Like velocity (but for different gesture types), gesture-repeat frequency often maps to emotional arousal (fast to increase, slow to reduce).	Heavily dependent on gesture and context
Compound	Movement pattern	The action or movement performed by the toucher	The specific motion used during touch, encompassing variations in spatial and temporal parameters, can contribute to the emotional message conveyed.	E.g., different characteristic movement patterns for stroke, pat, hug, tap [O]
	Approach	Rate, location and angle at which the hand approaches the touched surface	When perceptible from warmth, hair disturbance or other senses, it sets an expectation which alters eventual preception, and predicts contact force and velocity.	E.g., the approach of a full-hand slap may be fast and wide; a caress slow and wide; a tickle fast and narrow in extent.

Citation format: (Name'year, ..., Name'year, [attribution code])
^Attribution code: [S] Documented property of touched **skin**; **[M]** Estimated from touch sensor **modeling**; **[O] Our** estimated value, observation or definition; **[R]** From data reported in this paper, since **rarely reported** in literature

of research across disciplines. *Affective* touch has unique properties [14, 43, 63], an interplay of which creates a non-verbal language that can convey meaning beyond words; *e.g.*, a gentle, long, and soft touch on the arm can convey support from a friend, whereas a strong, short, and high-frequency tap from a sibling might signify a call for attention. These tactile interactions are often highly personalized [42], and the same touch sequence may convey different meanings or emotions to different individuals.

We can categorize these properties from a touch recipient's perspective. *Spatial properties* include where on the body contact occurs, its direction and spatial extent, contributing information about its location and orientation. *Temporal properties* describe timing and rhythm, including duration, velocity, repetition, and the frequency of repetitive touches. *Physical properties* include the materiality of the contact surface, (*e.g.*, stiffness, texture, temperature), stress, and intensity. By controlling these properties in interpersonal touch, humans build a social touch "language".

Researchers often study this language via "touch gestures" [17, 97]. In Table 1, we draw on past work to list these properties and the values that others have proposed or observed as pertinent in describing touch stimuli. While out of our present scope, we note the influence of external factors, including individual touch preferences, context, setting, timing, social relationship between toucher and touchee, and emotional history of the interaction. These nuances need to be considered when conducting human-subject experiments to understand this domain.

Table 2: Key technical properties for array-based surface sensors designed to capture affiliative affective touch. Colored boxes indicate our subjectively-applied ratings for the relevance of each sensor property to Table 1's affective touch properties. Where available, we have listed relevant values reported in the literature. This mapping shows what is needed to capture all the relevant touch properties; and can help to infer technical requirements for a specific application's needs.

			Spatial			Mechanical				Temporal				Compound		
	Affective Gesture Property (Table 1):		*Body location*	*Contact area & hand extent*	*Gesture length*	*Forcefulness*	*Stroke angle*	*Sliding contact*	*Stroke modulation*	*Duration*	*Velocity*	*Repetitiveness*	*Repetition frequency*	*Movement pattern*	*Approach*	
	Sensor Property	**Qualitative Description of Property**														**Related Efforts & (where available) Values Achieved**
Spatial	**Spatial resolution**	Intertaxel distance (taxels/unit area) is small enough to support required gesture detection	3	5	5	1	2	3	1	1	4	1	1	5	1	1 in / 7 gestures differentiated (Cang'2015, [M]) 1.5cm / 13 gestures (Choi'2022, [M]) 0.3mm; no gestures recognized (Devaraj'2019, [M])
	Inter-taxel deadzone	Minimization of any unsensed gap between taxels	2	4	4	2	3	5	5	3	3	3	3	4	1	Generally not reported.
	Cross-array measurement consistency	Degree to which variance in taxel readings **across the array** is minimized, at unstressed baseline and throughout taxel stress/output curves	3	4	4	4	4	5	4	3	3	2	2	5	2	Generally not reported.
	Multi-touch capability	Number of distinct touch points that can be simultaneously detected and individuated	3	4	4	4	2	4	1	3	3	3	3	5	2	100 (Cang'2015, [M]) 49 (Choi'2022, [M]) 16 (Devaraj'2020, [M])
	Touch proximity detection	The presence, distance and localization of a potential touching element in some specified range from the array surface.	3	2	1	1	1	1	1	2	2	3	3	3	5	Generally not reported.
	Overall sensor size & # of taxels	The total area covered by a single array, and # of taxels incorporated; greater area allows larger gestures and body location distinction	5	4	4	1	1	1	1	4	4	3	3	4	1	14x14 mm^2 (1 taxel) (Morton'2023 [M]) 95 x 95 mm^2 (36 taxels) [R] 10x10 in^2 (100 taxels) (Cang'2015, [M])
Mechanical	Normal Stress: **Saturation or max measured**	The **maximum** value at which **normal** stress can be sensed	2	2	2	5	5	2	5	3	3	3	3	5	2	Max reported stress applied: 1N (Tomo'2018, Parzer'2018, [M]) Max reported stress applied: 5N (Teyssier'2021, [M])
	Normal Stress: **Minimum detectable**	The rate of change of sensor output to applied stress, and linearity of that response	2	2	2	5	5	3	4	3	3	3	3	5	2	0.4 N detected change (Huisman'2013, [M]) 0.5 N detected change (Cang'2015, [M])
	Normal Stress: **Slope & linearity**	The **minimum** value at which **normal** stress can be clearly detected; important for light touch detection	3	3	3	5	5	2	5	3	2	2	2	5	2	0.48 kPa^{-1} (Lo'2020, [M]) 1.32 kPa^{-1} (Nie'2015, [M])
	Shear Stress: **Saturation or max measured**	The **maximum** value at which **shear** stress can be sensed, and **linearity** of the min-max range	2	2	2	5	5	2	5	3	3	3	3	5	2	Generally not reported.
	Shear Stress: **Minimum detectable**	The **minimum** value at which **shear** stress can be clearly detected; important for light touch detection	2	2	2	5	5	5	5	3	3	3	3	5	2	Generally not reported.
	Shear Stress: **Slope & linearity**	The rate of change of sensor output to applied stress, and linearity of that response	3	3	3	5	5	5	5	3	2	2	2	5	2	0.31 kPa^{-1} (Sarwar'2023, [M]) 0.01 kPa^{-1} [R] Not reported (Choi'2022, [M])
	Hysteresis and crosstalk	Degree to which inconsistency between stress application and release is minimized; including visoelastic effects	1	1	2	5	5	5	5	2	4	4	4	5	2	Hysteresis error: 0.57% (Wyss'2020, [M]) Hysteresis error: 5.6% (Guo'2016, [M])
Temporal	**Response latency**	Time from physical contact to stable output reading (electromechanical pipeline).	1	1	1	3	4	3	5	4	5	4	4	5	2	Complex to measure and generally not reported, although ultimately important in performance.
	Sampling frequency	Refresh rate of the entire array, or taxels/second; a factor of the control electronics and # of taxels in array	1	1	1	3	4	3	5	4	5	5	5	5	2	1225 taxels/s (Choi'2022, [M]) 2560 taxels/s (Devaraj'2020, [M]) 32 taxels/s (Fernandes'2021, [M])
	Temporal measurement consistency	Degree to which variance in taxel readings **over time** for the same applied stress is minimized	1	2	2	5	5	3	5	4	5	4	4	5	2	Minimal variance over 5 cycles (Fernandes'2021, [M]) Minimal variance over 10000 cycles (Sharma'2020, [M])

Other sensor properties not directly related to sensing of touch, but which are likely to have required values imposed by the specific application.

Other Properties	**Underlying surface stiffness**	Ability to retain accuracy when mounted on compliant as well as hard surfaces	**Material stretchability**	Ability to deform laterally to accommodate a dynamic surface, e.g., expanding, contracting, flexing
	Array configurability	Ability to support arbitrary shapes and patterns for non-rectilinear surfaces, including complex curves	**Material flexibility**	Ability to conform to non-flat surfaces; specifiable as radius of curvature in 1 or more dimensions

Rating meaning: The relevance of the information available from this sensor property to the affective touch property is **[5] direct and important; to [1] not informative.**
Citation format: (Name'year, …, Name'year, [attribution code])
^Attribution code: [S] Documented property of touched **skin**; **[M]** Estimated from touch sensor **modeling**; **[O] Our** estimated value, observation or definition; **[R]** From data reported in this paper, since **rarely reported** in literature

3.2 From Human to Technical Requirements

Table 2 translates parameters descriptive of human affective touch to technical sensing parameters and their likely needed range of values, such as spatial and temporal characteristics, sensitivity, adaptability, and reliability. Finally, the table provides values where these requirements have been reported. This is a non-exhaustive list but provides a framework for benchmarks of sensors designed for similar applications and denotes where values are rarely reported. We anticipate that exact needs will vary for many reasons already mentioned, including application context. Table 2's targets should be viewed as a starting point adaptable to specific situations.

4 SENSOR DESIGN

We substantially adapted previous approaches [34, 35] to create a soft flexible capacitive sensing array with 36 (6×6) taxels, overall size of 94×94mm^2, and 2mm thickness. Each 14×14mm^2 taxel has 3 axes (z normal and x-y shear stress), with 2mm between taxels. Our design prioritized low cost, manufacturability, flexibility and configurability, alongside sensing performance.

In overview, the sensor array is an elastomer matrix of deformable pillars sandwiched between (on top) transmitting electrodes (laser-patterned on stretchable conductive fabric), and receiving electrodes on a custom FPCB forming the array's bottom surface (Figure 2). We worked with large ranges of elastomer density and pillar design to adapt sensitivity and spatial resolution from previous high-stress applications (*e.g.*, 1mPa [96]) to the delicate levels exerted by affective touch (43kPa or 10N/taxel). The soft sensing stack has been demonstrated with 1D bending at a 10mm radius, limited by the FPCB base [61]. It is read by a compact custom microcontroller, featuring low power consumption and wireless connectivity; with a global sample rate of 43Hz with 2Mbps throughput, from a user's touch to receipt on an untethered control laptop. In §4.1, we provide full details of our own implementation. Some aspects are similar to [35], but not fully documented; others differ substantively.

This design's most salient improvements relative to [35] are:

Mechanical Design (§4.1.1): We used an inverted truncated pyramidal pillar structure rather than square pillars; and Ecoflex GEL as the compositing elastomer instead of the stiffer Ecoflex 00-30. Together these adaptations increased per-taxel sensitivity by 570%.

Array Size (§4.1.3): We devised 36 taxels rather than 16 to cover a larger area for three-axis stress sensing, targeting differentiation of one-hand gestures.

Modularity (§4.1.4): Although not demonstrated here, the current FPCB can be cut into any array smaller than 6×6. This adds versatility for soft sensing applications requiring smaller or differently-shaped sensing areas.

Virtual taxel for data augmentation (§4.1.5): Our new data augmentation approach improved the all-inclusive gesture classification model (§6.2.3, §6.3.1) by ~5% in accuracy by effectively tripling the number of taxels per unit area.

Manufacturability (§4.2.2): We improved alignment between T_x/R_x electrodes and thickness homogeneity by adding and modifying mould elements and steps, increasing sensitivity uniformity (§5.2).

4.1 Design Details

4.1.1 Taxel Structure. We employed a 5-channel parallel-plate capacitive taxel configuration (Figure 2), adapting the design from a shear sensing array for foot plantar-stress monitoring [34, 35]. Modifications to increase sensitivity and spatial uniformity included material (a much softer elastomer), dielectric pillar structure and inter-taxel spacing, resulting in a 5.7× increase in normal stress sensitivity (Supplement E, Figure E.1 & Table E.1).

Taxel size (14 × 14mm^2, similar to a human finger-pad) is comparable to previous shear sensing efforts [20, 21]; other properties are listed in Table 3.

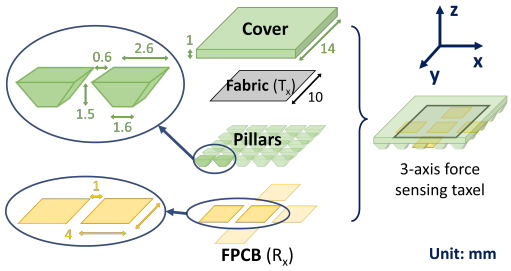

Figure 2: Layout of an individual taxel with electrode and pillar dimensions. Green regions are elastomer, yellow copper electrodes on the FPCB, and grey stretchable conducing fabric. Exploded view at left, full taxel on the right, with the black square showing the top (T_x) electrode, partially overlapping with the outer Rx electrodes to enable shear detection in 2 axes based on the differential signal.

Functionally, one square excitation electrode ("transmission" or T_x, patterned on conductive fabric, width w_t= 10mm) is embedded in an upper insulating elastomer layer; five square receiver electrodes (R_x, width w_r=4mm) are laid out on the underlying FPCB.

These layers are separated by 1.5mm-tall square, truncated-pyramid elastomer pillars with 1.6/2.6mm lower/upper edges. Qin *et al* [71] suggests that a pillar width/height ratio of $\sqrt{2}$ optimally balances sensitivity and linearity. As we sought this ratio, the pyramidal shape decreases shear stiffness relative to a rectangular pillar, for greater deflection and thus signal, while increasing normal force range. Concerns regarding PCB bonding led us to cut off the point. Taxels are separated by 2mm; air fills the non-pillar T_x/R_x gap.

Total structure height is 3mm including the elastomer structure, adhesive and FPCB.

4.1.2 Sensing Shear and Normal Stresses. Following [73], we computed three-axis stress using each taxel's 5 capacitance channels (rather than the 4 previously used). For this method, [73] found cross-talk of <5% from normal stress to shear signal, and <10% between shear axes [73].

Figure 3[a-upper] shows how overlap of the larger T_x electrode with the five R_x electrodes creates five corresponding capacitances 1–5, separated by a field of elastomer pillars. The blue dotted lines between T_x and R_x electrodes approximate the electric field in each channel, imposed by the potential difference across two terminals. Higher-density electric field lines mean high electric flux density and thus channel capacitance. When unloaded, T_x overlaps fully with the central electrode to generate the central capacitance C_3, and 50% with the four outer electrodes to form capacitances $C_{1,2,4,5}$.

The separating elastomer pillars are of height d_z when unloaded (Figure 3[a-lower]). Under a uniform normal stress, the electrode separation d_z decreases by ΔZ, while the overlap area, A_{ol} is unchanged for all electrodes; so C_{1-5} increase in inverse proportion to ΔZ. With an x-axis shear stress added, assuming T_x remains parallel to the R_x electrodes, C_2 decreases while C_4 increases due to their differing overlap (A_{ol}) changes. Meanwhile, C_3's A_{ol} is unchanged in the absence of accompanying normal stress.

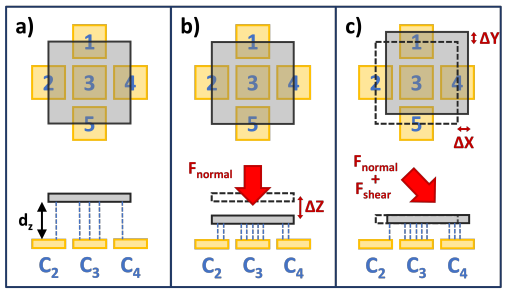

Figure 3: Principle of applied normal and shear stress translation to 5 capacitance channels. Top (upper) and side (lower) views of a single taxel's active elements under (a) no stress, (b) normal stress, and (c) normal stress plus shear. Dashed blue lines represent field, with more lines indicating higher capacitance. The dark grey square is the top electrode, which displaces vertically in (b) and laterally in (c), as indicated by the dashed black lines.

We calculate capacitance changes related to shear, labelled D_x and D_y [73] (as estimation of displacements ΔX/ΔY in two axes, Figure 3(c)) using capacitance differences across each axis:

$$D_x = \frac{C_5 C_1' - C_1 C_5'}{C_3'}$$
$$D_y = \frac{C_2 C_4' - C_4 C_2'}{C_3'}, \quad (1)$$

where C_n denotes the baseline (channel n) and C_n' the instantaneously measured (channel n) capacitances. These extracted signals are related to measured displacements and stresses via calibration (§5). In the normal stress direction, we report the capacitance change divided by the initial value, $C0$: $\Delta C/C0 = C_3' - C_3)/C_3$.

4.1.3 Array Design. To scale a single taxel to an array, a grid reduces electrical connections. T_x connections are shared by column (6 total); there are five R_x connections per taxel row (30 total). Figure 4 shows the FPCB and depicts the top layer of the exploded view in Figure 5. For example, a second taxel to the right of the first requires one new T_x connection but can re-use the first taxel's five R_x connections. Similarly, creating a new row of taxels, the T_x connections are re-used, and a new set of five R_x connections is added. The column is scanned by measuring capacitance between one T_x and each R_x connection, and the array is probed by repeating this for all T_x. The number of taxels, P, scales as the number of connections squared. Given a total of k connections including M T_x connections and N sets of 5 R_x connections (total $k = M + 5N$), the number of taxels, g in a square sensing array is:

$$P = M \times N = -5N^2 + kN. \quad (2)$$

The square sensing array used here has $M = 6, N = 6$ and a total of 36 connections. For our square array, the number of connections scales as the square root of taxel number times 6.

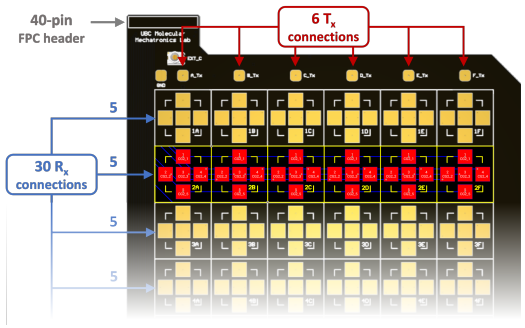

Figure 4: Sensor design. A 6×6 array of three-axis (normal & shear) stress sensing taxels are configured on a custom FPCB.

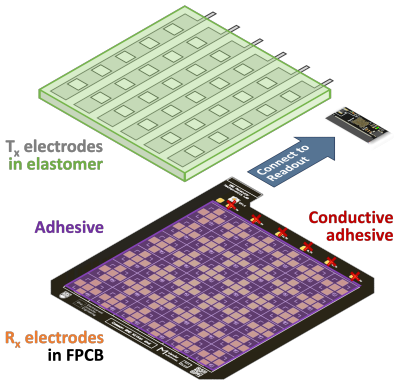

Figure 5: Array assembly. 6×6 normal/shear stress sensing array assembly and its connection to a custom microcontroller.

The T_x electrodes, fewer in number, are made from patterned strips of conductive and stretchable fabric on the sensor's top surface. The R_x features require finer and tighter connections, and so are patterned directly onto the flexible printed circuit board.

4.1.4 FPCB. Figure 4 depicts our 2-layer FPCB design with 6 T_x, 30 R_x, and 4 Ground connections that form the array's base. On top, 6 T_x copper pads align with the conducting-fabric electrodes. For each T_x row, 5 R_x-aligned copper pads are linked to traces on the bottom layer. Ground planes on both FPCB layers minimize parasitic capacitance. All T_x, R_x, and Ground connections are routed to the top-left of the FPCB's bottom layer, linking to the 40-pin 0.5mm pitch FPC header and thence a custom microcontroller.

4.1.5 Shear from Computed Virtual Taxels. To mitigate the effect of un-sensed inter-taxel deadzones, and also anticipating that higher spatial resolution could improve gesture recognition, we computed normal and shear values from adjacent outer channels of neighbouring taxels. We used these new clusters of capacitance channels as *virtual taxels*, a novel data augmentation method.

Specifically, we focused on the virtual taxels in the middle of 2 and 4 physical taxels (Figure 6), looking at the capacitance channels that overlap the area of a selected virtual taxel. Based on the ratio of the overlap, the original 5 capacitance readings involved in the

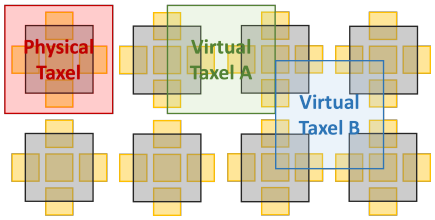

Figure 6: Virtual Taxels. The 6×6 three-axis stress sensing array is expanded to 11×11 by integrating the measurements from 2 (A) and 4 (B) adjacent physical taxels.

calculation of D_x, D_y, $\Delta C/C0$ for a physical taxel got replaced by a set of new capacitance readings. This effectively increases the spatial resolution in normal/shear stress by nearly 2 times, from 6×6 to 11×11. More information can be found in Supplement C.

4.2 Fabrication

Fabrication involves moulding the elastomer dielectric, cutting and patterning the conducting fabric T_x electrodes, bonding the layers to the FPCB, adding a shielding layer to remove interference from proximity signals, and bonding a soft elastomer cover layer.

4.2.1 Preparing Materials. We print four moulds in PLA using a FDM 3D printer (Prusa MK3S+): a base with square truncated-pyramid voids; an electrode alignment guide; and two base-mounted rails to control elastomer cover thickness. For the T_x electrodes, we use stretchable conductive fabric (silver-coated nylon from Less EMF) for ease of laser-cutting into arbitrary patterns using a Versalaser carbon dioxide cutter. We cut 6 conductive fabric strips, each with 6 T_x electrodes. We used Smooth-On Ecoflex™ GEL [1] for the elastomer cover and pillars, for its low durometer (the second softest material in the Ecoflex™ lineup, Shore hardness 000-35) to enhance mechanical deformation and thereby sensitivity.

4.2.2 Moulding. We fabricate the elastomer structures with embedded T_x electrode in four steps (Figure 7).

(1) Form elastomer pillars: 15g of Ecoflex™ GEL (Part A:B = 1:1) are poured into the base mould. Vacuum is applied to remove bubbles. Excess Ecoflex is scraped off. The pillar layer is cured for 2 hours at room temperature.

(2) Form layer embedding T_x electrodes: A thin bonding layer of Ecoflex is applied to the pillar layer, followed by a laser-patterned transparent film guide. The top electrodes (six T_x fabric strips) are inserted into the guide's cutouts and the guide is removed. Vacuum is applied, then a 2-hour cure at ambient conditions.

(3) Form elastomer cover: 10g of Ecoflex is poured, excess removed, then cured for 2 hours.

(4) De-mould: Excess Ecoflex is cut from the edges of the cured structure. The custom structure is then ready to attach to the FPCB.

4.2.3 Assembly. A non-conductive silicone-based adhesive (Silicone Solutions SS6004VF+) is applied to the elastomer pillars (Figure 5) before aligning each taxel's T_x electrode to the corresponding R_x electrodes. The T_x electrode strips are crimped with copper connectors and soldered to the FPCB.

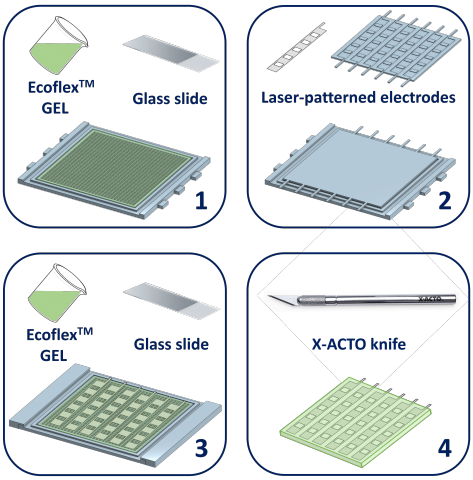

Figure 7: Fabrication process for custom elastomer structure with embedded T_x electrodes. (1) Form elastomer pillars; (2) embed patterned T_x electrodes; (3) form and level the elastomer cover; (4) demould.

4.3 Microcontroller Design & Control

A microcontroller measures taxel capacitances and relays them by Bluetooth to a computer or mobile device. It is electrically connected to the sensor array via an FPC connector (Figure 5).

4.3.1 Microcontroller Board Design. We achieved this form by adopting Infineon's Cypress PSoC-63 dual-core (160/100 MHz) microcontroller unit (MCU) in a 116-pin BGA package [2]. Its built-in capacitance sensing solution (CAPSENSE™) eliminated the need for external capacitance-to-digital converters (CDCs) commonly seen in embedded systems built for capacitive sensing. For wireless data transmission, we implemented PSoC's built-in Bluetooth Low-Energy (BLE) 5.0 solution by incorporating a chip antenna and a 32 MHz crystal oscillator. With an 8-layer PCB architecture, including resin-filled blind vias, our compact custom microcontroller is fast (up to 10,000 mutual-capacitance reads/s, wireless-capable (BLE 5.0; max 2Mbps bandwidth), and low-power (~20mW when scanning and wirelessly transmitting data).

4.3.2 Avoiding Parasitic Capacitance. Parasitic capacitance (coupling to within the board and to external objects such as fingers) increases the total reading, compromising the relative change caused by taxel deformation. On the FPCB, a ground plane is inserted between T_x and R_x traces that are on the same layer, and it is ensured that there is no overlap between layers. For the custom 8-layer microcontroller, it is ensured that none of the 40 FPC traces overlap with each other between adjacent layers. A ground plane is added to each microcontroller PCB layer to prevent the proximity of fingers or other from affecting the capacitive signal.

4.3.3 Firmware Logic. On the top layer of the microcontroller PCB is an FPC socket linking the array's 40 electrical connections (T_x/R_x/Ground) to pins in the PSoC 63 MCU (Figure 5). The firmware is programmed to scan the 6 T_x × 30 R_x= 180 pairs of

array measurement points. The MCU's built-in average filter (window size = 4 samples) and median filter (3 samples) reduce noise without significant impact on temporal response. The output is a 180-element array, *RawCounts*. Values proportional to the change of channel capacitances are packed into an array of integers, and transmitted to outer systems via BLE. Alongside the 180 *RawCounts*, additional CAPSENSE^{TM} parameters are also transmitted wirelessly to calculate the raw capacitance values (see Supplement B, Figure B.1 & B.2).

4.3.4 Data Capture Pipeline. Data collection and visualization consists of the FPC connector (sensor array to microcontroller), Bluetooth (to receiver board), and a USB cable (to PC) (Figure 8). The receiver (a PSoC-6 BLE Pioneer Evaluation Board) captures the microcontroller's data via BLE and passes it to a Windows 11 PC via a USB2 connection. Using Python, the timestamped data is saved. The PC calculates D_x, D_y (Eq. 1), given capacitance values converted from *RawCounts* and CAPSENSE^{TM} parameters.

A custom real-time visualization displays shear (D_x, D_y) with arrows indicating magnitudes and directions, and a heatmap of vertical capacitance change magnitudes.

4.4 Surface Material and Friction

The soft sensor array benefits from a surface covering, especially for the very soft elastomer and tacky elastomer used in this study. Exact needs vary with polymer softness and taxel sensitivity.

Protection vs. electromechanical transparency: The surface must be durable enough to protect the sensor from wear and tear, while flexible enough to cleanly transmit touch indentation and capacitance.

Friction for shear: If too slick, lateral (shear) stresses are not transmitted to the sensor unless unnaturally large normal stresses are applied (heavy touching). If too sticky, the contact cannot slide, or chatters unpleasantly.

Tactility: The surface texture should reasonably emulate the simulated surface (*e.g.*, skin or short fur); and be inviting to touch.

For the final sensor version and gesture collection (§6), we covered the sensor with a soft stretchable cotton fabric, 2mm thick.

4.5 Overarching Objectives & Outcomes

Sensor design was motivated by several high level goals.

Modular Design: We placed the FPC connection between the sensing array and the readout circuit, splitting electronics into two modules to reduce the cost, debugging effort, and effort of replacing the low cost FPCB. An option also exists to extend the FPC length by commercially available 40-pin cables and connectors, ncreasing options for real-time deployment. When the sensing array is worn out after long-time use, it can be replaced at a cost that is low relative to other technologies.

Low Cost: We estimate a per-system cost of ~20USD. This includes a ~15USD microcontroller (at 1000 pieces, with PCB manufacture and on-board component assembly); and <5USD for materials (laser-patterned conductive fabric electrodes, elastomer base and FPCB).

Low Power: Consumption is ~20mW (sensing system, ~43Hz sampling and wireless transmission), significantly lower than previous wire-transmission counterparts (600mW [20], 330mW [3, 21]).

Table 3: Sensor characterization summary. All values reported are for the same sensor version (Sensor B).

	Property	Value/Description	Section & Figure**
Spatial	**Fixed Sensor Spatial Properties**		
	Taxel size [mm^2]	14 x 14	Section 4.1.1 Taxel Stucture
	Inter-taxel deadzone [mm]	2	Section 4 Sensor Design (Intro)
	Number of taxels	36	Section 4 Sensor Design (Intro)
	Overall sensor size [mm^2]	95 x 95	Section 4 Sensor Design (Intro)
	Spatial resolution [1/mm^2]	0.004 (0.4 cm^-2)	Section 4 Sensor Design (Intro)
	Spatial Performance		
	Cross-array measurement consistency (Standard Deviation of the slopes [1/kPa])	7.6e-5 (8.5%)	Calculated based on Table SuppE.2
	Multi-touch capability	Yes (36)	N/A
Mechanical	**Fixed Sensor Mechanical Properties**		
	Sensor stiffness (z-axis): Effective Modulus [kPa]	58	Calculated based on Figure SuppE.2
	Sensor stiffness (x,y-axis): Effective Modulus [kPa]	1.5	Calculated based on Figure SuppE.3
	Normal Stress (measured as ΔC/C in response to applied normal stress [kPa]		
	Maximum stress measured [kPa]	43	Figure 11 a)
	Minimum detectable stress [kPa]	1.5	Figure 11 a)
	Slope [ΔC/C/kPa] Slope of linear portion of response/input stress curve	0.01 (< 10 kPa), 0.0008 (> 10 kPa)	Calculated based on Figure SuppE.4
	Goodness to the linear fit - Coefficient of determination [R^2]	0.99 (< 10 kPa)	Calculated based on Figure SuppE.4
	Repeatability (standard Deviation of the peaks of 300 cycles)	0.0017 (3.5%)	Calculated based on Figure 12
	Inter-taxel Z axis crosstalk	*No observed normal activation in adjacent taxels for applied z axis stress in central taxel*	Figure SuppE.6
	Shear Stress - Isometric lateral response *(measured as Dx and Dy in response to applied shear stress [kPa]*		
	Maximum stress measured (limited by setup) [kPa] (+2 mm to - 2 mm)	+- 3.8	Calculated based on Table SuppE.2
	Minimum detectable stress [kPa]	+- 0.3	Figure 11(b),(c)
	Slope[(1/kPa]	0.11	Calculated based on Table SuppE.2
	Goodness to the linear fit - Coefficient of determination [R^2]	0.994	Calculated based on Table SuppE.2
	Independence of shear from normal stress	*Shear sensitivity is largely unchanged with different normal force application*	[Sarwar'2023]
	Within-taxel X-Y Axis independence	*No observed activation of x-axis shear when y-axis shear applied, or vice versa.*	Figure 11(e)(f)
	Intra-taxel X-Y axis cross-talk	*No observed shear activation in adjacent taxels for applied x, y or z stress in central taxel*	Figure SuppE.7
Temporal	**Temporal properties**		
	Sampling frequency [taxel/s]	~ 1548 Hz	Section 4
	Sampling frequency [array/s]	~ 43 Hz	Section 4

**SuppE.# = Supplemental materials E, figure/table #

5 SENSOR PERFORMANCE

To connect this sensor's capabilities to the tentative targets from past descriptive studies of affective touch (Table 2), we carried out an extensive test battery which we hope will serve as a baseline for future touch-sensing efforts. These numbers are a snapshot representing one application with its design tradeoffs.

Table 3 summarizes characterization results for taxel performance in normal and shear stress, cross-array consistency, impact of the elastomeric material, and measurement repeatability. These are further discussed in §7.5 in light of our performance needs.

5.1 Characterization Methods

Figure 9 demonstrates our characterization setup, consisting of a THORLABS 3-axis NanoMax^{TM} 300 Flexure stage and an ATI SI-50-0.5 Multi-axis Force/Torque (F/T) load cell [72]. A flat 14×14mm^2 square-face indenter was printed and mounted on the load cell to provide uniform taxel compression. Prior to characterization, the array was taped to a custom-printed upper platform on the 3-axis stage, used to align the centers of the chosen taxel and the indenter. We then raised the stage to put the array in contact with

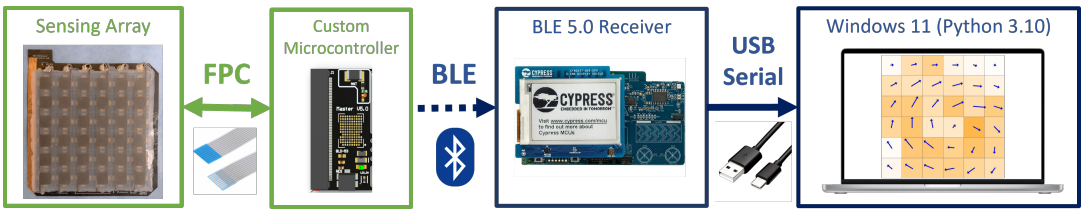

Figure 8: Hardware connection pipeline for collection and data visualization (Visualized gesture example: Circular Stroke).

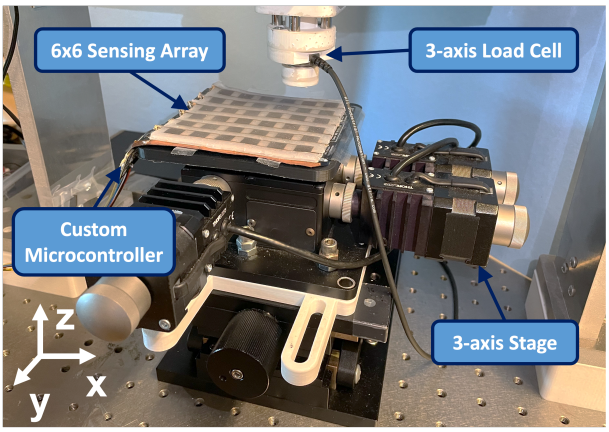

Figure 9: Sensor characterization setup. THORLABS 3-axis NanoMax^{TM} Flexure stage equipped with an ATI Multi-axis Force/Torque (F/T) load cell, used to apply normal and shear displacements to the sensor array.

the indenter at a normal stress of 2.5kPa for shear characterization and 2.5e-2kPa for normal direction characterization.

We simultaneously recorded the load cell's 3-axis force and the array's 180-channel capacitance readings on six representative taxels. This included the four most heavily used (B2, B5, E2, E5 – Figure 10): in piloting, most gestures were performed on the central taxels, and this region also showed the most use during formal data collection (§5.3). We therefore represented each 3x3 quadrant with its central taxel. We further examined taxel A1, representing a typical response from corner and near-connector taxels; and taxel C4 to compare sensor responses across surfaces with varying curvatures. These results are detailed in Supplement E, Figure E.12.

We defined a movement sequence for the 3-axis stage to validate the sensing array's ability in capturing shear touches: the x-axis/y-axis offset of each taxel was incremented from 0mm to 2mm (the sensor's designed 2mm shear limit) every 3s in 0.2mm steps. After the last step, the stage moved the taxel to its origin (offset = 0mm). This procedure was performed in all four shear directions.

Displacement speed was $2mm/s$ (acceleration $2mm/s^2$), with no holding at local peaks. These were chosen to complete incremental peaks within 2s, to align with the gesture data collection window of §6.1. The normal stress characterization followed a similar protocol, with the upper limit at 0.8mm, corresponding to 40% shear strain.

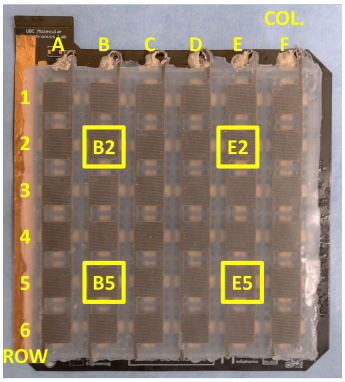

Figure 10: Taxels chosen for shear characterization. Array columns are referenced as (A-F), rows as 1-6.

5.2 Performance Test Results & Analysis

We report the sensing uniformity among the characterized taxels in the three-axis stress readings, as well as sensitivity and measurement range for individual taxels. To assess the Ecoflex^{TM} elasticity, we measured hysteresis in single-taxel normal stress readings with displacement-controlled compression cycles.

5.2.1 Normal Stress. Figure 11(a) presents normal stress response over time. An initial stress of 0.15kPa was applied to ensure proper contact, followed by an increase to ~66% (normal stress of 43kPa). Baseline capacitance is 2.2pF (maximum change 0.24pF). Figure 11(d) shows the stress response at different displacements: a strong linear relationship between the sensor reading ($\Delta C/C0$) and displacement.

Figure 11(b) exhibits good linearity between the shear stress reading and displacement; a linear fit has a slope (sensitivity) of $0.08mm^{-1}$ with R^2 of 0.98, an excellent fit. However, Figure 11(a) shows a a nonlinear relationship between normal stress and sensor reading ($\Delta C/C0$). Therefore, we applied two linear fits to the two operating normal stress ranges (Supplement E, Figure E.4). In the low normal stress range (<9.3kPa), we see a slope of $0.01kPa^{-1}$; then a lower sensitivity of $6.2\times10^{-3}kPa^{-1}$ in the high-stress region (9.3kPa<P<43kPa). This is unsurprising: the pillar design creates the air void structure in which a small stress can cause a large displacement change. However, the pillars are compressed almost to saturation, increasing the compression modulus.

Sensor hysteresis is another consideration. The red-circled region on Figure 11(a) reveals shear relaxation as position is held constant following the final force ramp. This leads to apparent hysteresis phenomenon (Supplement E, Figure E.5) when the change in

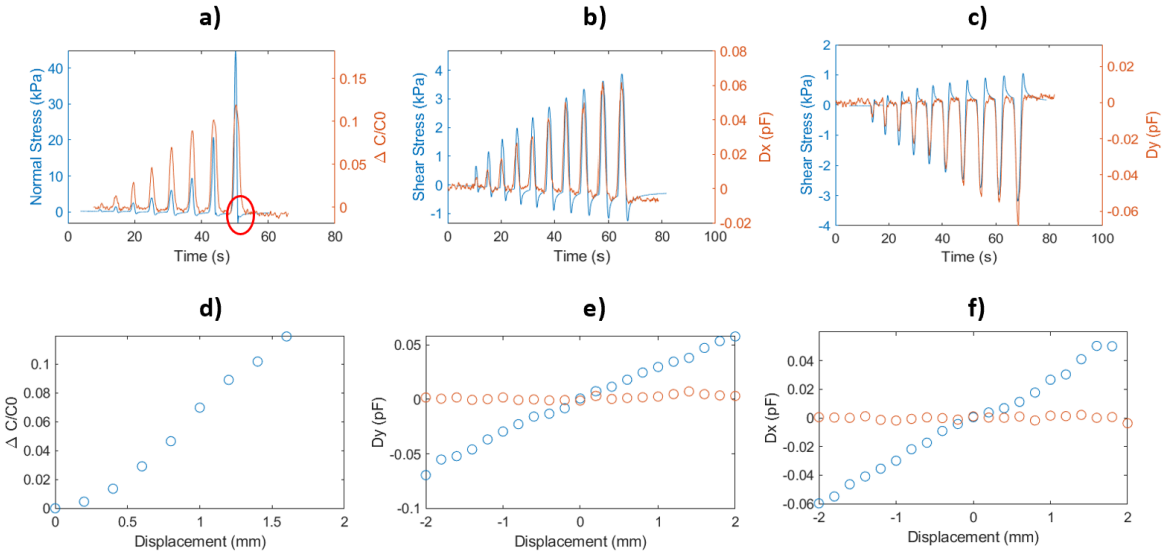

Figure 11: Normal and shear stress characterization – linearity and channel independence. Shear response (D_x) as a probe horizontally shears a single taxel with non-sliding (isometric) contact from the taxel's center to 2mm displacement in 0.2mm steps (~2 s). Directions are normal (left), negative x (center) and negative y (right). The red circle indicates shear relaxation.

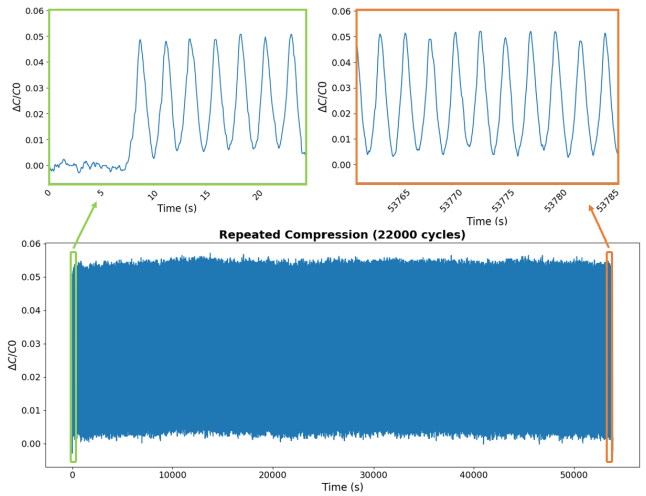

Figure 12: Normal stress Repeatability. A sensor taxel underwent 22000 normal-stress cycles over 14 hours. The two upper callouts show the similarity between the start and end of this test.

position or force is fast compared to relaxation rate (approximately 3s here). When the indenter is rapidly pulled up, a delay in the return of the material to its original state leads to a sudden drop in normal stress This effect is not seen under position control. The main implication is a slight delay in the drop in normal stress at removal of contact. As a result, very fast and repetitive gestures, such as piano playing or quick finger-tapping, may not be fully captured. In our study, this could affect movements like tickling.

5.2.2 Shear Stress. Figure 11(b) and (c) present a sample test result wherein a normal contact force of 0.5N (2.5kPa) is applied to prevent the indenter from sliding on the sensor's surface. Baseline capacitance is 2.2pF (maximum change ± 0.05pF). In Figure 11(a), (b) and (c), the sensor's shear stress reading is depicted by the blue curve, while the red curve represents the load cell reading, converted to kPa. Following each local peak, the shear steps return to 0mm, with an observable offset in the shear reading equivalent to 0.2mm or 10%. This offset likely results from slippage at high shear displacement, but may also have a viscoelastic contribution, and in use could manifest as a phantom light or increased touch following the application of heavy shear, especially over a prolonged period. The offset disappears once contact with the surface is removed.

Figure 11(e) and (f) display the sensor's shear reading *vs.* the displacement. Each blue dot represents the reading at a specific applied shear direction, while red dots indicate shear readings (crosstalk) for the perpendicular direction. Blue dots are derived from local displacement peaks, and corresponding red dots from crosstalk at those specific times. The blue datapoints show strong linearity within the characterized range of -2mm to +2mm; therefore, we applied a linear fit to these data, and found an R^2 (coefficient of determination) of 0.99, signifying an excellent fit.

Its slope indicates the sensitivity in the unit of kPa^{-1}. Specifically, the slope for x-axis shear is 1.2×10^{-2}pF*kPa^{-1}(0.11 kPa^{-1}), with a range from -3.8kPa to 3.9kPa and a minimum detectable shear stress of ±0.6kPa. For y-axis shear, it is 1.3×10^{-2}pF*kPa^{-1} (0.12kPa^{-1})), covering -3.2kPa to 3.8kPa, also with a threshold stress of ±0.3kPa.

The results for all four taxels are summarized in Supplement E, Table E.2. The average slope of the four characterized taxels is 1.2×10^{-2}pF*kPa^{-1} (0.11 kPa^{-1}), with a standard deviation of 0.01×10^{-2}pF*kPa^{-1} ($9.4 \times 10^{-5} kPa^{-1}$). In computing average and

standard deviation, taxel B2 was excluded due to its notably low sensitivity compared to the others, which likely indicates damage from previous testing. Figure E.12 (E) shows a typical response of a taxel positioned at the corner and near the connector (Taxel A1), which has sensitivity of (x-axis) 1.3×10^{-2}pF*kPa^{-1} ($0.12kPa^{-1}$) and (y-axis) 1.9×10^{-2}pF*kPa^{-1} ($0.18kPa^{-1}$). The edges deform somewhat more easily in shear due to lack of neighbors, with the x-axis less sensitive than the y-axis, likely due to the stiffness of the crimped electrical connection to the FPCB in that direction. Crosstalk between shear axes is 10% at most. This will lead to some small apparent shear on perpendicular axes, potentially shifting the shear vector by about 6 degrees.

5.2.3 Effect of Curvature on Shear Sensitivity. We mounted the sensor array on surfaces of 80mm (forearm) and 30mm (thumb) radii, with the axis x-aligned (Supplement E, Figure E.8). Sensitivity increased in the x-axis by 20% and 30%, respectively, while in the y-axis it decreased by 6% and 20% (Supplement E, Figure E.9-E.11 & Table E.3). In the x-axis (along the ridge) sensitivity increases because the lower indenter contact area increases normal stress for the same applied force, creating a larger capacitance, and hence a larger change in capacitance [61]. In the y-axis, the capacitances observed when normal stresses are applied drop, from 3.40pF flat, to 3.30pF at 80mm and 3.20pF for the 30mm curvature, since these regions are not as heavily compressed. Later, we show that gesture classification works on a soft, curved surface (§6.3.3).

5.2.4 Repeatability. An Instron Universal Testing Machine (Model 5969) applied 22,000 normal-direction stress cycles to a single taxel over 14 hours (peak normal stress 16kPa; Figure 12). Motion was continuous with no hold time at peak or trough.

We would expect to see some shift in maximum and minimum signals due to material softness, but there should not be a clear changing trend in overall signal shape. The test showed a standard deviation of 0.0015 (2.8%) in the maximum per-cycle change, showing minimal persistent effects of force cycling for this period. §5.3 also describes sensor condition after >5000 gestures.

5.3 Failure Assessment

The sensor (A) on which 12 of 16 reported participants' data was collected (§6.1) underwent 26.5 hours of use, including characterization, pilot testing, and multiple iterations of data collection. After this extensive use, it was replaced (Sensor B) for the final 4 reported participants (7 hours use after its characterization and data collection). 3 participants' data was discarded and replaced by these 4, due to excessive anomalies. The characterization data presented in Table 3 is from Sensor B.

We believe much of Sensor A's damage occurred in bursts; one of its last users was particularly forceful.

The damage applied to the middle 9 (most heavily used) taxels. The top Ecoflex layer wore out in this region, exposing the top electrode to the air. The pillars underneath were broken, and had debonded from the FPCB. The implication of this failure mode is that shear stress causes the sensor layer to shifted to a new position on the FPCB without returning, a form of inelastic deformation.

We describe possible mitigations in Supplement A.

6 GESTURE CLASSIFICATION & EVALUATION

To test the ability of the 6×6 sensing array to capture essential features of affective touch gestures throughout its iterative development, we developed a protocol to collect gesture instances from multiple individuals, then used its data to train a variety of machine-learning models. In all, we ran versions of this protocol 3 times, adapting it with respect to gesture set, constraints on gesture performance and gesture segmentation, as well as sensor version and modeling approach, as we strove to understand the complex interplay between touch-generated normal and shear stresses and how to coax these out of the sensor. Reported here is the final version of that protocol and analysis of its dataset (N=16, 9 gestures) using a custom 3DCNN model. To better understand how the 3DCNN might be arriving at its predictions, we implemented a set of handcrafted features on participants' data and reported significant differences observed between participants and between gestures.

6.1 Gesture Data Collection

For the final gesture set that we report here, we recruited 16 participants (15 right-handed, 1 left-handed, 8 female, 8 male, aged 21-30 years) for 1.25-hour (75 min) sessions, compensated $15 for their time. This protocol was carried out under approval of the University of British Columbia's behavioral ethics approval #H15-02611-A021.

6.1.1 Gesture Selection. We selected 9 gestures to address several considerations:

Ecological validity: Diverse representation from Yohanan *et al* (2012)'s naturalistic social touch dictionary [97].

Data richness and classification challenge: Representation of shear as well as normal stress activation, and including items that vary in morphological properties and in between-gesture similarity from easily confusable to easily distinguished.

Comparability: Subset-consistency with past sensor-based studies of social touch (*e.g.*, [17, 21]).

Classification challenge vs. practicality: A total set-size of 8-10 – slightly larger than most past works but still collectable in a single participant session without undue fatigue.

These gestures are listed and described in Table 4, along with their variation on several relevant morphological properties to illustrate the set diversity. Notably, *Back & Forth Rub*, *Isometric Rub* and *Circular Stroke* are similar in temporal dimension but differ in sliding contact, rotation and gestural travel.

6.1.2 Gesture Constraint and Instructions. Gestural constraints can co-vary in many factors, such as instruction (oral *vs.* video; detail on heaviness of touch, gestural extent, shape, orientation; enforcement), orientation relative to sensor, and gesture trial segmentation. One possible spectrum for co-varying these factors to balance naturalism with logistic and technical modeling challenge is:

Zero: Fully naturalistic and continuous touching with no instructions outside of the provided context.

Minimal: Participants given gesture description; instructed to perform single gesture continuously over a timed period.

High: Participants shown textual descriptions and video demonstrations of the gestures (as implemented by [21]).

Table 4: Gesture Definitions provided to participants, mapped to Gesture Properties adapted from Table 1. The range of ratings in each column (subjective by authors) demonstrates diversity of how this gesture set "exercises" each gestural dimension.

		Spatial			Mechanical							Temporal		
Gestural Dimension: *(capturing most relevant affective touch properties, Table 1)*		*Contact area*	*Hand extent: fingers / palm*	*Gesture travel*	*Forcefulness*	*Angle: Of finger contact*	*Angle: Normal stress engaged*	*Angle: Shear stress engaged*	*Angle: Rotation*	*Sliding contact*	*Stress modulation*	*Duration*	*Velocity*	*Repetitiveness*
Gesture	**Definition provided to participants**													
Poke	Using one finger, poke the sensor repeatedly	1	1	1	5	5	5	1	1	1	2	1	5	5
Wide Pinch (w_pinch)	Using 2-4 fingers, make one inward pinch that is at least 2 finger-widths apart, release the pinch within the 2s trial	3	3	3	4	3	4	5	3	4	2	2	3	1
Heavy Pat (h_pat)	With the flat of your hand, pat the sensor repeatedly as through you are heavily patting your leg	5	5	1	3	1	5	1	1	1	3	2	4	5
Twist	Anchoring 2-5 fingers on sensor, twist your fingers in place more than 90 degrees repeatedly	3	3	2	4	4	3	5	5	2	3	3	2	4
Back & Forth Rub (b&f_rub)	Using 3-5 fingers, rub the sensor back and forth with your fingers sliding	5	4	5	3	1	3	5	2	5	4	5	3	5
Isometric Rub (iso_rub)	Anchoring 2-5 fingers on sensor, jostle fingers back and forth in-place, as if rubbing a bruise on your leg	2	3	1	4	2	3	5	1	1	5	5	3	5
Circular Stroke (cir_stroke)	Rub the sensor in circles with the flat of your hand, allowing your hand to slide	5	5	4	3	1	3	5	5	5	4	5	3	5
Tickle	Using as many fingers as you like, lightly tap the sensor as though you are tickling someone	4	4	3	1	4	1	2	1	2	4	2	5	4
Constant Touch (constant)	Place the flat of your hand on the sensor	5	5	1	2	1	2	1	1	1	1	5	1	1

Rating: The degree to which a gestural dimension applies to a gesture definition: **[5] high degree** (e.g., many fingers, high force relative to other gestures); **[1] little to none.**

Since we are at the stage of establishing sensor requirements and needed segmented data, but also wanted our data to contain features representative of natural affective touch, for the reported gestural dataset collection we used a "moderate" level (between *minimal* and *high*) wherein participants were instructed to 'imagine performing each gesture as they would naturally on their leg,' perform the gesture repeatedly within a 2s trial (except for *Pinch*) and to interpret otherwise the definition provided in (Table 4) as best they could. Overall the definitions of gestures were well understood. However, *Tickle* was confusing for 3 participants and *Isometric Rub* was confusing for all participants. In these instances, the experimenter performed the gesture on their leg and asked participants to copy it as best they could from the visual demonstration.

Over our many collection iterations, we varied these factors extensively to identify modeling sensitivity to their variation. Two protocol improvements proved helpful. First, we focused participants on performing more or less the same gesture, so as to avoid overwhelming the model with irrelevant data variation, by offering visual demonstrations when participants were confused by the description (as opposed to simply naming the gesture as described earlier). Secondly, we shortened trial time from 9s to 2s for a single gesture (this unit is also referred to as a "data instance" in analysis, below). This way any large individual differences in the 9s data instances that the model was unable to recognize, was mitigated.

6.1.3 Collection Study Design. Data collection was segmented by trials, wherein a trial consisted of repeated performance of a gesture for 2s (unless otherwise specified by the definition). Trials were performed in 9-gesture blocks (one gesture/trial, with gesture-trial order randomized per block). Each participant performed 52 blocks, for a total of 468 trials (data instance). The full dataset is thus composed of 52 blocks × 1 trial × 9 gestures × 16 participants = 7488 instances of gesture data. In the user study, we collected 7581 data instances. This difference was resulted from repeated trials or minor errors (*e.g.*, participant failed to record the correct gesture at first and had to redo the gesture). From the 7581 instances, we used 7315 (96.49%), based on the second step in the data preprocessing described in Table 5.

We determined data needs for our 3DCNN classification model via iterative piloting. 2s trials best captured one full gesture performance. 468 trials (all gestures) require a non-onerous 15.6min per participant of contact time. For efficiency comparison, Skin-On Interfaces (UIST'2019) [85] models 8 gestures (320 trials, trial duration not provided) with efficient image processing techniques. Our 3DCNN, chosen to handle 3D temporal data, requires more data. Choi *et al* [21], with a CNN, capacitive shear+normal stress sensor, used approximately double this data in 5s trials (29.3min per participant).

6.1.4 Procedure. During a study session, participants were told about the study, completed the consent process and were provided with instructions about performing the gestures. A collection session took about 75 minutes.

Participants were seated in a desk chair facing the sensor (placed in the same orientation with the microcontroller connection on the top left side) on a hard flat surface, near their dominant hand, and with a laptop and monitor screen in front of them (Figure 13). The sensor was covered with a white cotton fabric chosen to provide enough slip on the sensor's surface for gestures that required sliding friction and to protect the sensor's top gel layer.

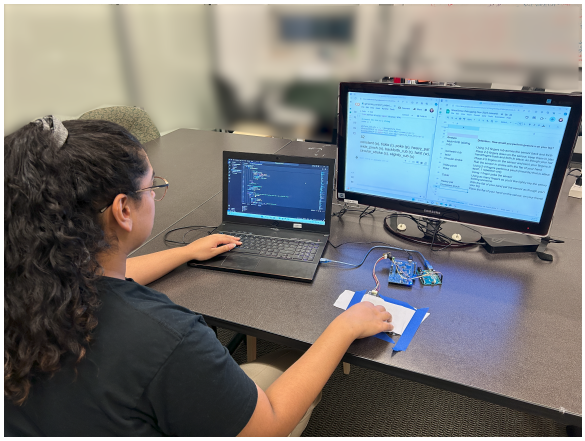

Figure 13: Gesture collection study setup.

They were first introduced to the sensor with 10s of *Free Play* (freely touching the sensor to reduce the interaction's novelty). To capture the 2s trial participants had to begin performing the gesture as they pressed a corresponding key on the data collection laptop with their non-gesturing hand. After 2s they would hear a beep from the computer to indicate that the 2s trial is over and they can perform the next gesture. The monitor screen showed the list of gestures to perform in the current block along with the unique key to press, the gesture descriptions, what gestures had been previously performed, and what block number they were currently at. Example photos of gestures being performed with the corresponding visualization can be found in Supplement D.

During collections, a researcher monitored the process and asked participants to repeat a gesture if they noticed a large deviation from the gesture definition. E.g. for *Twist,* if participants did not twist their fingers more than 90 degrees, the experimenter would request them to repeat the gesture. After 12 blocks, participants took a 2m+ break to minimize fatigue. We also checked in periodically for self-reports of fatigue, which no participants indicated.

6.2 Machine Recognition Pipeline

6.2.1 Organizing Raw Data. After collecting data from all 16 participants, we organized the raw data for the 9-class classification with deep learning (pipeline shown in Figure 14). Within each participant's folder were one or more CSV files corresponding to segments within their data collection session. Within each CSV file (§4.3.4), raw sensor data was first filtered by the custom microcontroller's built-in average and median filters, collected as 180-channel *RawCounts* (180 columns), alongside CapSense™ parameters (1 column) for capacitance calculation, and timestamps (1 column). To facilitate extraction of gesture instances for deep learning, we added a gesture label (1 column) and a touch flag (1 column), expanding the CSV size to (184, n).

6.2.2 Preprocessing. The goal of the preprocessing (steps in Table 5) was to effectively extract valid gesture data, calculate the normal/shear stress measurements at 36 taxel locations, and prepare them for loading to our custom deep learning model.

Table 5: Preprocessing steps for the machine recognition pipeline. For each CSV data file, we included the D_x, D_y, $\Delta C/C0$ data for both physical taxels and virtual taxels, generated NPZ files of sizes (3, 86, 11, 11), and stored them in 9 gesture instance folders.

Step	Process
1	Split file into multiple 2-second data instances according to the logged gesture labels and touch flags.
2	Screened out gesture data chunks that have too many (>96) or too few (<76) samples — the sample number varied due to wireless data transmission.
3	Linearly interpolated the remaining data chunks (96.5% of the total) in time to be 86 samples each.
4	For each sample, calculated capacitance values for the 180 channels as discussed in §4.1.2.
5	Obtained D_x, D_y, $\Delta C/C0$ for the 36 taxels according to each taxel's 5 capacitance values.
6	Adopted virtual taxel implementation, as explained in §4.1.5, to create taxel readings (D_x, D_y, $\Delta C/C0$) between the existing 6×6 taxels to reach an array size of 11×11.
7	Saved the expanded array of quantified taxel readings (10-bit integers; 1024 levels with level 0 being zero normal) as gesture instances in the NPZ file format with a size of (3, 86, 11, 11) each.

After including the D_x, D_y, $\Delta C/C0$ data for both physical taxels and virtual taxels, we generated NPZ files of size of (3, 86, 11, 11) and stored them in 9 gesture instance folders.

6.2.3 Data for classification. We utilized the 3DCNN model [21, 45, 74] to tackle aspects of our research questions. From RQ3: Can shear stress data facilitate ML classification? From RQ4: Are these 9 gestures, with verbal definition shown to the participants, generalizable between at least the 16 studied individuals? If so, the potential exists for a classification model that can effectively distinguish anyone's gestures (from the 9 studied gestures) without further training with the new stress data.

All-inclusive: To tackle RQ3, we randomized the gesture instances in each of the 9 gesture data folders, followed by a 70/20/10% data split (train/validation/test). The train and validation gesture instances were then joined between the folders respectively, ready to be loaded to the 3DCNN.

Leave-one-out: For RQ4, we implemented a 70/30% data split (train/validation) for 15 participants' data and reserved the last participant's data only to test the trained model. This was done for P1-16, leading to 16 datasets prepared for the 3DCNN.

6.2.4 Gesture classification using 3DCNN. We constructed a custom 3DCNN (Figure 15), used for both all-inclusive and leave-one-out (LOO) modelling tasks. It consisted of an input layer, 3 three-dimensional convolutional (Conv3D) layers, 1 global average pooling (GlobalAveragePooling3D) layer, and 2 fully-connected (Dense) layers inserted with 1 dropout layer. The reason for the increased number of convolutional layers and filters, compared to prior work [21, 74], was the higher amount of data stored in each data instance. Coming from the input layer, the first Conv3D layer had a kernel size of (1, 1, 43), a stride of (1, 1, 4), and a filter number of 128. The kernel and stride were set to condense the time-domain information, so the output could have balanced dimensions—(11, 11, 11)—in the hope for better feature extraction in the following Conv3D and fully connected layers. The second and third Conv3D layers

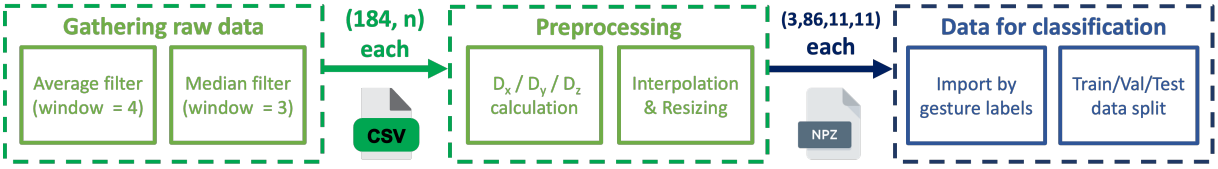

Figure 14: Preparation of data for the 9-class gesture classification using a 3DCNN.

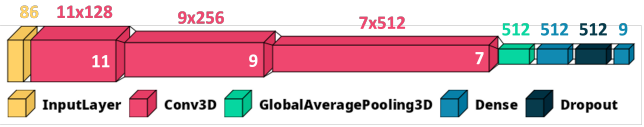

Figure 15: Custom 3DCNN for gesture classification. Following Visualkeras [36]. For illustration purposes, the model visualization is not to scale, and the three batch normalization layers, each following one Conv3D layer, are omitted.

shared a kernel size of (3, 3, 3) and a stride of (1, 1, 1), but differed in the number of filters—256 and 512. Batch normalization was performed after each Conv3D layer. The third Conv3D was followed by the GlobalAveragePooling3D layer, the first Dense layer, and the dropout layer—all of the same size (512). The output was then fed to a 9-neuron Dense layer to generate the probability matrix of predicted gestures.

Regarding our all-inclusive model, depending on the input data, we altered the number of channels of 3DCNN's the input layer – 1 for normal stress only data, 2 for shear stress only data, and 3 for three-axis stress (normal and shear combined) data. For the leave-one-out model, in comparison, the number of channels was fixed at 3 since we only used three-axis stress data.

Before starting on the training, we set a learning rate of 0.00001 and a loss function using categorical crossentropy. In addition, an Adam optimizer and early stopping callback (patience = 15; max number of epochs = 200) were adopted.

6.3 Results

6.3.1 Overall accuracy. For both all-inclusive and leave-one-out models, we ran 5 rounds and training and testing. Here we report their respective overall accuracy and gesture-related findings.

All-inclusive: Among 5 rounds of results, the median overall test accuracies (Figure 16(d)) are 80%, 79%, and 88% respectively for models trained and tested with normal-only, shear-only, and three-axis data. Therefore, to classify the 9 gestures defined by our study, the three-axis data model outperforms the other two. Using the test data from three models, we present their normalized confusion matrices (CMs) in Figure 16(a-c). From them, we noticed that, three-axis model yielded the highest classification accuracy for 6 out of 9 gestures. The three gestures for which normal-only and shear-only models performed better than the three-axis were *Wide Pinch* (normal-only by ~5%), *Poke* (shear-only by ~14%), and *Twist* (normal-only by ~1%).

Leave-one-out: A leave-one-out cross-validation approach (Figure 17) revealed an average accuracy of 64% (SD ± 27%) for the generalized three-axis model, with each participant serving as test data five times as described in §6.2.3. Although we saw relative moderate classification accuracies for three participants (P3, P8, P14; each with a 5-round median >75%, compared to chance – 11%), the substantial variation between the rest suggests the model may struggle to capture the unique characteristics of unseen participants with different traits, potentially limiting its generalizability. Confusion matrices for the LOO analysis can be found in Supplement D, Figure D.3-D.4.

6.3.2 Relative Shear and Normal Stress Contributions to Accuracy. To analyze the effects of 'Channel' (three-axis, shear-only, or normal-only) and 'Gesture' on test accuracies. we employed a two-way Aligned Rank Transform (ART) ANOVA [93], given that our data violated the assumptions of normality and homogeneity of variances for a regular ANOVA.

The analysis revealed a significant main effect of 'Channel' ($F(2, 144) = 17.64$, $p < 0.001$). This indicates that test accuracies differed significantly across the different channel types. However, 'Gesture' ($F(8, 144) = 2.80e\text{-}29$, $p = 1.00$) and the interaction between 'Channel' and 'Gesture' ($F(16, 144) = 1.73e\text{-}30$, $p = 1.00$) did not show any statistically significant effects.

Post-hoc tests using Tukey's HSD further confirmed significant differences in test accuracy between the 'three-axis' group and both the 'normal-only' (mean difference = -2.0, $p < 0.001$) and 'shear-only' groups (mean difference = -2.0, $p < 0.001$). Interestingly, there was no significant difference in accuracy between the 'normal-only' and 'shear-only' groups (mean difference = 0.0, $p = 1.00$).

6.3.3 Gesture and Individual Differences. To gain a deeper understanding of the data, we extracted five key metrics from each participant's gesture execution. These were calculated based on 50 observations sampled for each participant-gesture pair. All measurements were normalized to 0-1 for consistency across participants. Table 6 summarizes how each metric was calculated.

To quantify differences within these metrics, we employed a Generalized Linear Model (GLM). The decision to use a GLM was driven by the nature of our data, which violated the assumptions of normality and homogeneity of variances that are required for many traditional statistical tests. This analysis was conducted using the Python libraries 'patsy'[2] and 'statsmodels' [76].

Procedure: Initially, we created contrast matrices for both the gesture and participant variables. The contrast coding scheme used was the 'sum' contrast, which compares each level of a categorical variable to the mean of the subsequent levels. This was done for all unique gestures and participants in our normalized measures dataset.

[2]https://patsy.readthedocs.io

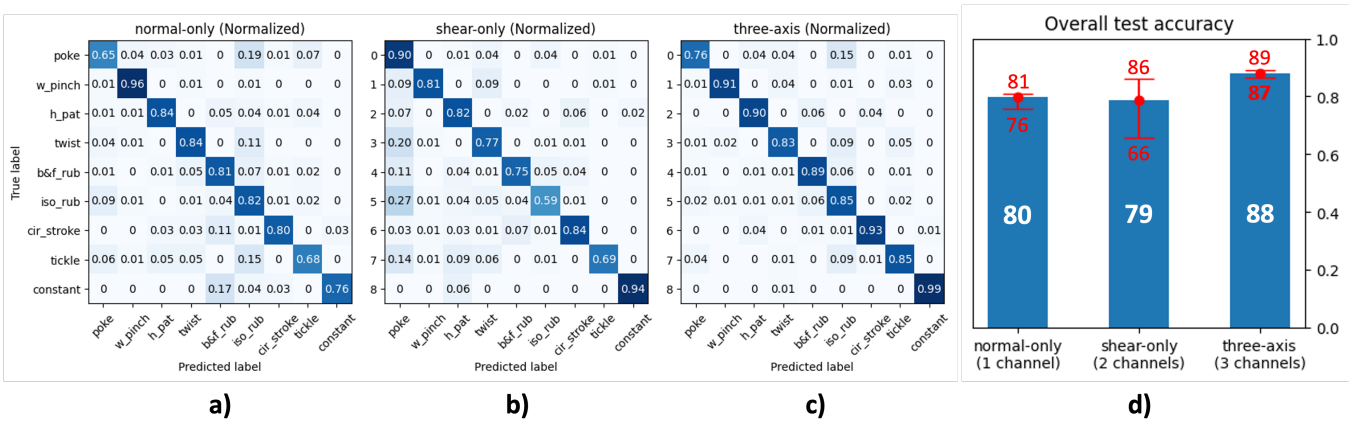

Figure 16: Test results for all-inclusive 3DCNN models. a) CM from the model trained and tested with 1 channel of normal stress data. b) CM from the model trained and tested with 2 channels of shear stress data. c) CM from the model trained and tested with 3 channels of three-axis stress data. d) 5-round median test accuracy of three models with respective minimum and maximum.

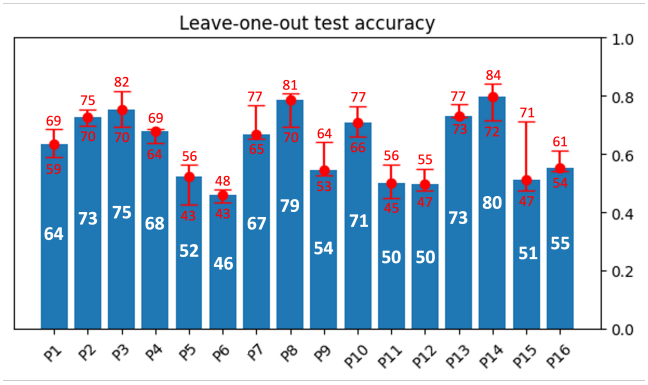

Figure 17: Test accuracy for leave-one-out models. Each is trained with 15 participants' data and tested with 1 reserved participant's data. The x-axis label indicates the data left out from training.

Subsequently, for each measure under investigation, we constructed a GLM. The model was specified such that the measure was the response variable, and it was modeled as a function of the gesture and participant factors. The gesture and participant variables were treated as categorical, with their contrasts defined by the previously created contrast matrices. The GLM was fitted to our normalized data using the Gaussian family.

Our primary objective is to understand and summarize the individual differences in how participants interact with the sensor during various gesture executions. Hence, we focus on individual variability, prioritizing the analysis of main effects for participants and gesture types.

Gesture Differences: We summarize the key findings for each extracted feature, visualized on Figure 18, investigating the effects of different gesture types.

Table 6: Key metrics for participant gesture execution & calculation details. Metrics are calculated based on 50 observations sampled for each participant-gesture pair. All measurements were normalized to 0-1 for consistency across participants.

Metric	Calculation Summary
Average Normal Stress	An activation threshold was first established at 5% of the maximum stress recorded across all participants. The average stress exerted by a participant on the sensor surface was then calculated for each sample, considering only the "activated" taxels (those exceeding the stress threshold).
Absolute Shear Magnitude	Similar to the average normal stress, the average absolute magnitude of the shear stress in the x and y directions was computed for each sample. This metric considers the magnitude of shearing stress acting on the sensor surface during the gesture execution.
Average Contact Area	The total number of activated taxels (those exceeding the activation threshold for pressure or shear for a majority of the time window) was summed to determine the average contact area. This metric provides insights into the surface area engaged during the gesture.
Maximum Frequency	As a proxy for the gesture dynamics, the maximum frequency (capped at 5 Hz) of summed pressure and shear signal was identified using a Fast Fourier Transform (FFT), capturing the dominant frequency component associated with the gesture execution.
Movement Type	The predominant movement type during the gesture was categorized as either "Transversal", "Convergent", "Divergent", or "Mixed/Static". This classification was achieved by analyzing the change in shear magnitude over time. If all changes were consistently positive (or negative), the movement was classified as "Transversal". An average positive change indicated "Convergent" movement, while an average negative change signified "Divergent" movement. Gestures without a clear directional trend were categorized as "Mixed/Static".

- *Average normal stress applied:* All gestures except *Back and Forth Rub* (p=0.606) exhibited a significant difference (p<0.001) in average normal force compared to the reference gesture.
- *Average absolute shear stress magnitude:* Similar to average normal stress, all gestures except *Poke* (p=0.081) showed a significant difference (p<0.001, p_{constant}=0.048) in average absolute shear stress magnitude compared to the reference gesture.

- *Average contact area:* Every gesture type analyzed *(Back and Forth Rub, Circular Stroke, Constant, Heavy Pat, Isometric Rub, Poke, Tickle,* and *Twist)* demonstrated a significant difference ($p<0.001$, $p_{poke}=0.040$) in average contact area compared to the reference gesture.
- *Maximum frequency (speed of gesture execution): Back and Forth Rub, Circular Stroke, Constant, Heavy Pat, Poke,* and *Twist* displayed a significant difference ($p<0.020$) in maximum frequency compared to the reference gesture. In contrast, *Isometric Rub* ($p=0.532$) and *Tickle* ($p=0.491$) did not exhibit a statistically significant difference.
- *Movement type:* All gestures showed a significant difference in movement type compared to the reference gesture ($p<0.020$).

Individual Differences: We observed a range of individual differences for each of the metrics derived from participants' gesture data, summarized in Figure 19.

- *Average normal stress applied:* A significant difference ($p < 0.001$) in average normal stress was observed between the reference and all participants, except for P6, for whom we did not observe a statistically significant difference ($p = 0.267$) compared to the reference participant.
- *Average absolute shear stress magnitude:* Similar to average normal stress, all participants, with exception of P9 ($p = 0.057$) and P10 ($p = 0.681$), differed in average absolute shear stress magnitude compared to the reference participant ($p < 0.001$).
- *Average contact area:* The analysis revealed a significant difference ($p < 0.001$) inthe average contact area between the reference participant and all participants, with exception of P7 ($p = 0.679$).
- *Maximum frequency (speed of gesture execution):* With exception of P3 ($p = 0.130$), P5 ($p = 0.496$), P7 ($p = 0.106$), P11 ($p = 0.825$), and P15 ($p = 0.507$), we observed a significant difference between all other participants' maximum frequency compared to the reference participant.
- *Movement type:* The analysis indicated a significant difference ($p < 0.020$) in movement type between the reference participant and participants P2, P3, P4, P5, P7, P8, P11, P12, P14, P15, and P16. For the remainder, we did not observe a significant difference ($p > 0.193$).

6.3.4 Testing the Sensor on a Soft Curved Surface. As a preliminary step to verify the sensing array's performance when mounted on a curved and soft surface, we taped the 6×6 sensing array to a 3D-printed, 125mm diameter cylinder covered with 1cm-thick soft foam, and collected a session from one new participant (P17) using the same procedure described in §6.1.4 (see Supplement D Figure D.1 for images of heatmap and gesture performance on this curved setup). We then carried out only the leave-one-out (LOO) analysis (§6.3.1), using P1-16's data for training and validation and P17's data for testing. We did not perform the all-inclusive analysis due to the 16x difference in flat/curved surface data volume.

Five LOO rounds achieved a median test accuracy of 51% (minimum 44%, maximum 58%). Although this median is lower than the *average* (64%) of the 5-round median test accuracy for P1-16, it is comparable to the five lowest individual flat/hard surface performances (medians 52, 46, 50, 50, 51% for P5,6,11,12 and 15 respectively), and considerably better than chance (11%). While more data is obviously needed to differentiate effects of individual and surface condition, and to establish exactly what is happening structurally within the sensor to increase or diminish sensitivity for softness and curvature; but this quick look is promising in terms of versatility.

7 DISCUSSION

We start by returning to the research questions articulated in §1.2, then expand on design considerations and future potential for this sensor technology learned through this development experience.

7.1 RQ1: What qualities of affective touch gesture data are enabled by this novel sensor technology?

7.1.1 Identification of Technical Requirements. In Table 2, we proposed important technical properties based on observed human touch characteristics, and reported a few values that have been achieved and reported in past work (sometimes for other applications with different needs). Most properties have not been reported on at all.

By way of validating targets, we observed that the sensor prototype used here captured shear and normal stress well enough to (a) demonstrate good signal range across normal touch levels, (b) differentiate a carefully curated gesture set, and (c) reveal nuances in gestural and individual differences. The values we report thus arguably comprise initial minimum requirements.

7.1.2 Priorities for Sensor Improvement. We believe that capture would be further improved by an even lower minimum-detectable stress threshold (both normal and shear), and by addressing issues accompanying the final soft sensor material (for performance, quickening of the viscoelastic response; and for usage, gaining control over surface tactility). While robustness was reasonable for an early prototype, greater durability is needed for different kinds of studies. These are further discussed in Supplement A.

7.2 RQ2: How well can affective touch data from this technology be modeled?

In summary, the three 3DCNN all-inclusive models (normal, shear, and combined) are effective at classifying gestures. The three-axis stress model in particular shows 88% accuracy for the 9 gesture classes, in contrast to chance (11%), and an improvement over normal stress only and shear stress only, at 80% and 79% respectively (§6.3.1). To this we added modeling of individual and gestural differences. We examine this result for novelty and limitations, along with ways to address them.

7.2.1 Results in Context. This performance is consistent with the improvement to 78% accuracy achieved by Choi *et al* [21] (a 3DCNN model for 13 gesture classes when including both normal and shear forces, compared to 66% without shear). Choi *et al*'s work was enabled by recent advancement in magnetic sensing, as ours is with soft capacitive sensing. We compare our soft flexible sensing array against this work in three respects.

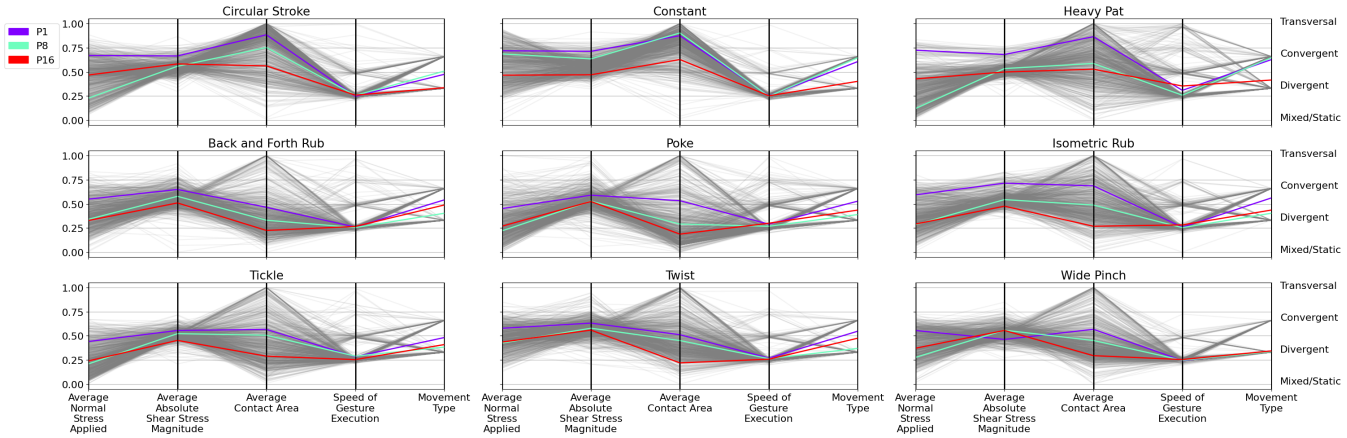

Figure 18: Normalized individual-participant data for each gesture. In a parallel coordinates plot, average execution of a given gesture for participants P1, P8, P16 are highlighted in bold colors to track their feature involvement across by gestures. The x-axis displays several of the data's numeric features; the y-axis gives the features' the normalized values. Movement types *(Transversal, Convergent, Divergent, Mixed/Static)* are indicated in equally-spaced plot ranges (*e.g.*, Mixed/Static = [0, 0.25]). Line spread reveals the degree to which model features captured diversity in participant and gesture.

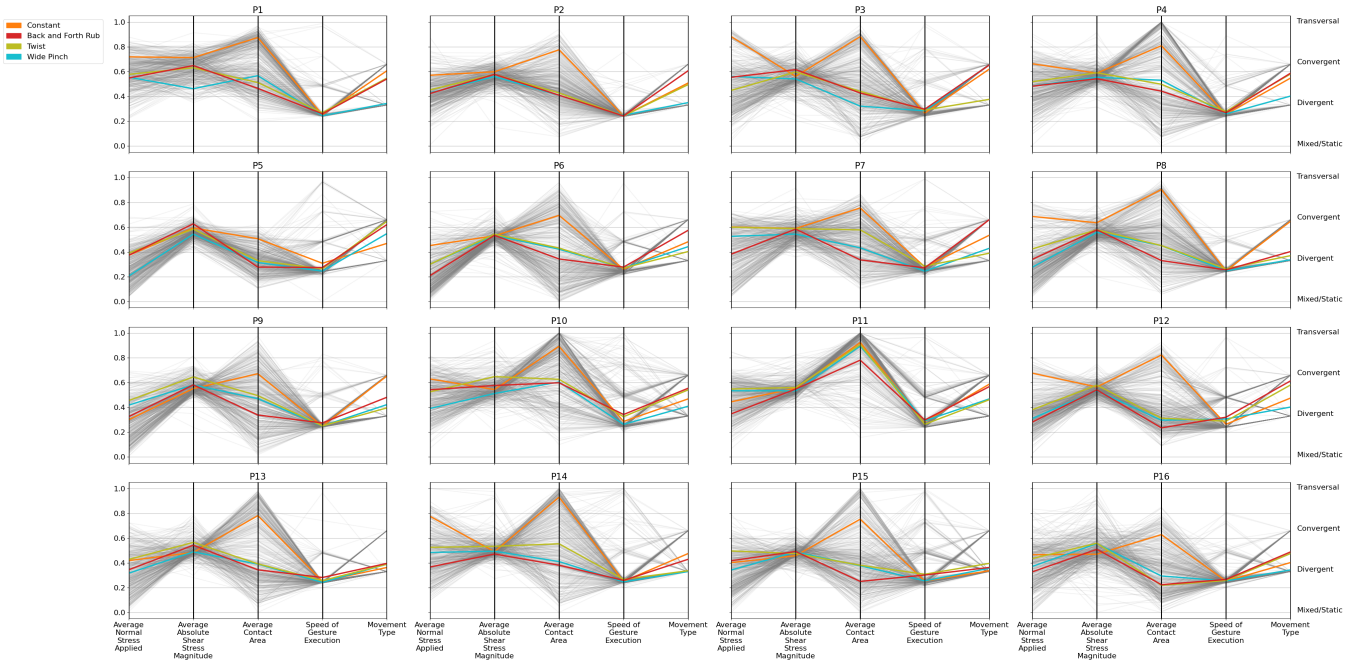

Figure 19: Parallel coordinates plot of normalized data for each participant. Each line represents a gesture, with an average representation of a gesture highlighted (*Constant, Back and Forth Rub, Twist, and Wide Pinch*) in bold colors.

Smaller hardware size (portability, intrusiveness): Our electronics minimize physical footprint, cost and power consumption, compared to Choi *et al*, where off-the-shelf magnetic sensors and a Teensy 4.1 Cortex M-7 microcontroller (readout dimensions $61\times17.78\text{mm}^2$). In comparison, our custom microcontroller's footprint is 72% smaller. Our three-axis stress sensing array is also thinner (<3mm compared to Choi *et al*'s ~8mm).

Moderately controlled gesture instruction: In an attempt to balance capturing a natural range with needed control, we prompted the participants with written gesture descriptions. Our individuals analysis confirmed that there was considerable inter-person variation in performance. We would describe Choi *et al*'s approach as more fully controlled (gestures demonstrated by video), but without an

individual analysis or assessment of variation, we cannot say how much this impacted their results.

ML Modeling: Our 3DCNN model added complexity – 3 Conv3D layers instead of the 1 and 2 used in Choi *et al* [21] and Sarwar *et al* [73] – to handle increased per-instance data delivered by our sensor collection protocol.

Individuals and gestures: Our individual and gestural analyses are the first of their kind for shear-based classification. This analysis of stress magnitudes, and varied stress utilization across individual and gesture, is unique contribution of the current work, that can be used by the community to further quantify gestures and improve sensor design.

7.2.2 Limitations on Model Findings. In the following, we examine how these modeling results can inform about naturalistic touch, and pave the way to better models.

Naturalism of modelled data: Our data collection procedure sought to elicit a natural range of expression, but obviously did not capture fully natural social touch. Participants were in a lab setting, touched on a flat surface, and were somewhat instructed in gesture performance. Further, as for the majority of emotional touch recognition work to date, they were not in emotionally authentic situations; gestures were performed, rather than being natural, emotional expressions.

Choice of gestures modeled: Table 4 shows how we intentionally diversified design of our gesture set. The gestures' evident use of different classification features (§6.3.3 generally confirms actual gesture diversity). However, it is self-evident that a larger set with more similar members would present greater challenge.

Potential of model approach: The 3DCNN model is a black box, unrevealing of the features that are important in distinguishing gestures. Several factors in our data and collection prohibited classical modeling with trained weights (§6.2.2), and the implemented 3DCNN model has more than 4 million parameters.

However, the raw data is a resource that can help test classification methods, and indicate where the sensor needs improvement. By computing characteristics such as net magnitude of shear, direction, time variation, area of contact, it should be possible to dramatically simplify and also speed model computation.

7.3 RQ3: What does shear add to normal stress and localization data in gesture recognition performance?

Our priority in this research was to understand *shear*: learning how to extract accurate shear stresses from human touch gestures, and getting insight into how shear manifests in these gestures and whether this information can assist in classification of gesture.

In 7 out of 9 gestures, shear alone or a combination of normal and shear measurement resulted in equivalent or better performance than normal measurements alone. Likely explanations involve both the direct information provided by the shear computation, and the added information as a result of 5 channel sensing.

7.3.1 Most Informative Features. Unable to interpret the inner workings of a 3DCNN, we analyzed the relationship between sensor data and model performance to reveal how individuals influence the data and, consequently, model recognition accuracy. Our analysis of features extracted from sensor data underscored the diversity of even these moderately-constrained touch interactions.

We found that most gestures varied substantively in normal, shear and spatial parameters compared to average execution across all participants; in particular average normal stress, average absolute shear stress, and average contact area. All gestures exhibited a unique movement type. Additionally, range in maximum frequency indicates the importance of gesture speed in interaction analysis.

These findings confirm the importance of a sensor able to capture this diversity – including shear as well as normal stress and spatial features; and model them with temporal history.

7.3.2 Overall Shear Contribution. Our study demonstrates that incorporating all three axes of touch data, including shear stress, leads to significantly higher accuracy in touch pattern recognition compared to using only normal or shear stress alone. This suggests that the additional information captured by shear plays a crucial role in differentiating subtle variations within gestures.

Intriguingly, there wasn't a significant difference between using only normal stress and only shear stress for gesture classification. This might indicate that emotional cues are expressed through subtle changes in shear stress that aren't fully captured by normal stress alone. While normal stress might encode the basic form of a gesture, shear stress could potentially capture finer variations in touch patterns that are linked to emotional expression.

The chosen gesture set, while exhibiting a range of "closeness", likely shares some underlying characteristics. For instance, back-and-forth rubbing gestures displayed higher shear stress values (§6.3.3), suggesting a link between shear and dynamic movement. Interestingly poke gestures, despite low shear variability, achieved significantly higher detection accuracy with shear data. This suggests that shear stress might be particularly informative for distinguishing static gestures (like pokes) from those with more movement (like rubs). Conversely, for gestures like rubbing that rely heavily on shear for differentiation (as evidenced by the lower performance with normal stress-only data), incorporating shear data becomes even more critical to capture the inherent variations within this gesture class, leading to more nuanced recognition.

7.3.3 Next Steps. To further investigate the relationship between shear stress and emotional touch, several avenues of research should be explored. First, the touch data should be labeled with corresponding emotional states during data collection, allowing for a direct assessment of how shear stress correlates with different emotional experiences. Additionally, feature engineering techniques focused on extracting characteristics of shear stress changes over time or its interaction with normal stress could provide more informative features for emotion recognition. Finally, training classification models using the extracted features and emotional labels would help determine if including shear data improves the ability to classify emotions from touch data.

7.4 RQ4: What kinds and degree of human individual differences do we see in gesture performance, even with moderately constrained affective gestures?

7.4.1 Overall individual variation. The individual differences which we observed at a high level were unsurprising. Individuals seem somewhat idiosyncratic from one another across their entire session's data, in that LOO accuracy varies. From this we infer that (a) individualized models may be important (or at least, user types); and (b) a larger database with more individuals will improve the situation (it becomes more likely that there will be another individual in the set that is more like you). As an indication of this, our own results were still improving as we added our 16th individual.

7.4.2 Individuals' Variability in Their Use of Shear. At a more fine-grained level, we also looked at the variability with which individuals employed shear relative to how they used normal stresses in gesture performance (§6.3.3). This analysis strengthens the case for individualized models.

The results reveal substantial individual differences in terms of average absolute shear stress magnitude compared to normal stress. While the GLM analysis for gesture effects showed a significant difference for all gestures (except *Poke*), the individual participant analysis is more nuanced. For example, P9 and P10 exhibited no significant difference in shear usage from the all-participant average, suggesting they might present more variability in normal stress; in turn, models built on these two participants would likely benefit more from the normal stress channel. Clearly, individual profiles can deviate from overall gesture trends.

These findings support the notion that a one-size-fits-all model might not capture the full spectrum of user interaction. By incorporating participant-specific characteristics, such as their personal balance between shear and normal stress usage, individualized models could potentially improve recognition accuracy.

Future investigations could explore the underlying reasons behind these individual differences. Factors like hand size, dexterity, prior experience with touch interfaces, or gender and cultural norms might influence how people do their touching.

7.5 Design Considerations

This project spans 4 major sensor revisions, 3 formal gesture-data protocols, and a substantially evolved modeling pipeline. In Table 7, we summarize the design's current limitations and challenges — spanning basic sensor design issues like sensitivity and shear/normal stress decoupling, scaling and versatility, modeling and verification, and practicality — then articulate goals and strategies which became apparent during our own process. Supplement A (Design Considerations) has further details.

8 CONCLUSIONS AND FUTURE WORK

This work sought to craft a sensor that is able to capture the nuanced way in which people carry out affective touch, prior to deploying such a sensor in authentically emotional, unconstrained environments where it is deployed on a physically interactive surface. To this end, we iteratively revised an existing technology, while using its ability to deliver data able to distinguish a carefully chosen set of gestures as an indication of its converging suitability for detecting nuanced elements of affective touch.

Key to our approach is the supposition that *shear* stress is one of these important elements, even though it has been rarely measured because of the technical challenge. Part of our objective, therefore, was to see if it was worth the effort.

The data we collected clearly demonstrates that shear is crucial, perhaps even more so than normal stress, even with the technology's current limitations. We propose a full set of technical properties that seem to be important in observed human affective touch, many of which are rarely reported or even sensed. This list is aspirational, but this work has begun putting numbers to it.

Technically, we found that shear is especially hard to capture for light touch – but light touch, for both normal and shear, is crucial to its value in this regard.

Finally, the sensor's ability to effectively capture subtle variations in touch gestures is promising as a window into the individualism of emotion expression, crucial to accurate modeling of affect in touch data.

Future Work: This work adds to the promise of using touch sensing to infer changes in emotion state; for example, in the context of human-robot or human-object interaction, for therapeutic, self-calming or emotive social communication purposes.

Challenges briefly touched upon in Table 7, and further expanded upon in supplement A, when addressed, will improve issues of performance, suitability, flexibility and robustness. With better, validated and faster models, we will be ready to attempt realtime control for responsive applications.

Stepping back, this project has given us confidence to deploy this technology in authentic-emotion experimental scenarios, which will in turn yield more valid data for modeling, both generally and for individualized models.

ACKNOWLEDGMENTS

This project was an adventure inspired and carried out as an interdisciplinary collaboration (haptic HCI and materials science) in labs with very different expertise and culture over its 6 years. We thank our patient gesture-study participants, Zavary Koehn for assistance on the sensor visualization, and feedback from UBC's UULab and SPIN Lab. This research was enabled by support from NSERC (Natural Sciences and Engineering Research Council of Canada), Calcul Québec, and the Digital Research Alliance of Canada.

REFERENCES

[1] [n. d.]. *Ecoflex™ GEL Product Information.* https://www.smooth-on.com/products/ecoflex-gel/
[2] [n. d.]. *PSoC™ 6 MCU: CY8C63x6, CY8C63x7 Datasheet, PSoC™ 63 MCU with Bluetooth® LE.* Available online.
[3] [n. d.]. Teensy® 4.1. https://www.pjrc.com/store/teensy41.html
[4] 2022. *Choose or Fuse: Enriching Data Views with Multi-label Emotion Dynamics.*
[5] 2023. *A Descriptive Analysis of a Formative Decade of Research in Affective Haptic System Design.* Association for Computing Machinery, New York, NY, USA Hamburg, Germany.
[6] Joshua M. Ackerman, Christopher C. Nocera, and John A. Bargh. 2010. Incidental Haptic Sensations Influence Social Judgments and Decisions. *Sci.* 328, 5986 (2010), 1712–1715.
[7] Saad Albawi, Oguz Bayat, Saad Al-Azawi, and Osman N Ucan. 2017. Social touch gesture recognition using convolutional neural network. *Computational Intelligence and Neuroscience* 2018 (2017).
[8] Kerem Altun and Karon E. MacLean. 2014. Recognizing affect in human touch of a robot. *Pattern Recognition Letters* November (2014), 31–40.

Table 7: Summary of design challenges and approaches for effective shear stress sensing design and evaluation. For articulated challenges, goals (•) are connected to (↜) strategies in sensor design, data collection and machine recognition (Supplement A for details.)

	The Challenge	Sensor Design	Gesture Data Collection	Recognition Pipeline
Decoupling Shear & Normal Stress	Shear and normal Stress are mechanically linked: a minimum normal stress must be exerted to engage shear. However, they are different parameters which sensor design must decouple in order to use both effectively later in the pipline. Specifically, normal stress must be detectable with zero shear, and shear across a range of normal stresses.	• Reduce mechanical and electrical cross-talk between capacitance channels ➤ Subtle adjustments in sensor geometry design. • Minimize deadzones and smooth out nonuniformities ➤ ``Virtual taxels'' offset the differential mechanical coupling that arises from touch contact away from taxel center. • Optimize finger-sensor mutual friction ➤ Careful choice of surface covering (\eg slightly grabby fabric)	• Validate sensitivity and cross-axis independence ➤ Gesture set with diversity in activation of shear and normal stress	N/A
Minimizing the Normal Stress Detection Threshold	High sensor sensitivity is required to capture the naturally delicate pressures naturally used in affective touch gestures.	• Reduce stiffness through geometry ➤ Pyramidal rather than square pillars • Reduce stiffness through material ➤ Reduced elastic modulus of elastomer • Tacky surface ➤ Use adhered surface covering • Tradeoffs (Future Work): capacitance saturation and reduced durability	• Confirmation that sensitivity is issue, rather than ML recogntion ➤ "Heavy gesture" collections improved models, motivating investmented in increasing sensor sensitivity.	N/A
Sensor Size, Resolution & Scaling	There is currently a soft physics-based limit on lower taxel size; meanwhile, resolution and spatial coverage are a tradeoff, with total taxel number constrained by multiplexed sampling rates. This array technology eases configuration to smaller, larger, arbitrarily shaped and linked layouts.	• Reduce taxel width ➤ Reduce layer thickness with different material and/or fabrication method. • Increase resolution in software ➤ Calculate virtual taxels • Eased demolding of soft components ➤ Use non-rectangular pillars • Arrays with configuration options ➤ Vary taxel spacing on FPCB; cut FPCB array down to any shape; daisy-chain multiple arrays to cover more space at same resolution.	N/A	• Increase model performance ➤ Higher resolution data from virtual taxels and denser arrays
Multi-Axis Flexibility	Affective touch will often be performed on complexly curved surfaces. Ideally, sensors will have multi-axis flexibility without substantive loss of performance. The current flexible PCB base allows just one bending axis.	• Achieve nonuniform shape confirmation ➤ Introduce 'kirigami' cuts into the PCB [28, 91]. • Achieve uniform general flexibility ➤ Eliminate PCB altogether [72].	N/A	N/A
Robustness	At 26.5 hours of use, our final test sensor showed signs of wear. Its failure points were debonding and soft material damage.	• Strengthen bonding ➤ Investigate different material approaches. • Increase elastomer durability ➤ Adjust tradeoff between sensitivity, structure and materials.	N/A	N/A
Pipeline & Modeling	We aim ultimately for continuous, realtime processing of live data with personalized models. Currently, we collect gesture data in delineated samples, and seeking explainability through multiple models pursued in parallel.	N/A	• Continuous collection ➤ Requires new segmentation algorithms • Emotion expression ➤ Authentic emotion elicitation [18].	• Continuous-data modeling ➤ Will require new live modeling methods. • Effective, understandable models ➤ Chosen after more analysis of a variety of approaches, on emotion data.
Debugging	A complex data pipeline (sensor -> data collection -> machine learning) made it difficult to ascertain issues.	• Identify issues with source data ➤ Perform sensor ``wellness checks''	• Locate issues throughout pipeline ➤ Institute data quality monitoring at multiple points	• Quickly try new model configurations ➤ Fast collection via streamlined protocols and accessible participant pool.
Practicality	Key to practicality is replacement cost \vs length of use. The reported prototype began to degrade at 26.5 hours of use, with the failed component replaceable at <$5 USD (6×6 array).	• Support longer unmonitored deployments ➤ Improve robustness (above) • Support longer overseen deployments ➤ Improve replaceability and parts costs	• Support longer unmonitored deployments ➤ Plan modeling for reduced amount of touching involved "in the wild"	N/A

[9] Kerem Altun and Karon E MacLean. 2015. Recognizing affect in human touch of a robot. *Pattern Recognition Letters* 66 (2015), 31–40.

[10] Deanna S. Asakawa, George H. Crocker, Adam Schmaltz, and Devin L. Jindrich. 2017. Fingertip forces and completion time for index finger and thumb touch-screen gestures. *Journal of Electromyography and Kinesiology* 34 (2017), 6–13. https://doi.org/10.1016/j.jelekin.2017.02.007

[11] Philipp Beckerle, Risto Kõiva, Elsa Andrea Kirchner, Robin Bekrater-Bodmann, Strahinja Dosen, Oliver Christ, David A Abbink, Claudio Castellini, and Bigna Lenggenhager. 2018. Feel-good robotics: requirements on touch for embodiment in assistive robotics. *Frontiers in neurorobotics* 12 (2018), 84.

[12] Clementine M. Boutry, Marc Negre, Mikael Jorda, Orestis Vardoulis, Alex Chortos, Oussama Khatib, and Zhenan Bao. 2018. A hierarchically patterned, bioinspired e-skin able to detect the direction of applied pressure for robotics. *Science Robotics* 3, 24 (nov 2018). https://doi.org/10.1126/scirobotics.aau6914

[13] Rachael Bevill Burns, Hyosang Lee, Hasti Seifi, Robert Faulkner, and Katherine J. Kuchenbecker. 2022. Endowing a NAO Robot With Practical Social-Touch Perception. *Frontiers in Robotics and AI* 9 (April 2022), 840335. https://doi.org/10.3389/frobt.2022.840335

[14] Rachael Bevill Burns, Hasti Seifi, Hyosang Lee, and Katherine J. Kuchenbecker. 2020. Getting in touch with children with autism: Specialist guidelines for a touch-perceiving robot. *Paladyn, Journal of Behavioral Robotics* 12, 1 (Dec. 2020), 115–135. https://doi.org/10.1515/pjbr-2021-0010

[15] Laura Cang, Paul Bucci, and Karon E. MacLean. 2015. CuddleBits: Friendly, Low-cost Furballs that Respond to Touch. In *Proceedings of the 2015 ACM on International Conference on Multimodal Interaction*. ACM, Seattle Washington USA, 365–366. https://doi.org/10.1145/2818346.2823293

[16] Xi Laura Cang, Paul Bucci, Jussi Rantala, and Karon E MacLean. 2020. Discerning Affect from Touch and Gaze During Interaction with a Zoomorphic Robot Pet. *IEEE TRANSACTIONS ON AFFECTIVE COMPUTING* (2020), 14.

[17] Xi Laura Cang, Paul Bucci, Andrew Strang, Jeff Allen, Karon MacLean, and H.Y. Sean Liu. 2015. Different Strokes and Different Folks: Economical Dynamic Surface Sensing and Affect-Related Touch Recognition. In *Proceedings of the 2015 ACM on International Conference on Multimodal Interaction*. ACM, Seattle Washington USA, 147–154. https://doi.org/10.1145/2818346.2820756

[18] X. Laura Cang, Rúbia Reiss Guerra, Bereket Guta, Paul Bucci, Laura Rodgers, Hailey Mah, Qianqian Feng, Anushka Agrawal, and Karon E. MacLean. 2023. FEELing (key)Pressed: Implicit Touch Pressure Bests Brain Activity for Modelling Emotion Dynamics in the Space Between Stressed & Relaxed. *IEEE Transactions on Haptics* early access (2023), 1–8.

[19] Carissa J. Cascio, David Moore, and Francis McGlone. 2019. Social touch and human development. *Developmental Cognitive Neuroscience* 35 (2019), 5–11. https://www.sciencedirect.com/science/article/pii/S1878929317301962

[20] Ming-Yuan Cheng, Chun-Liang Lin, Yu-Tse Lai, and Yao-Joe Yang. 2010. A Polymer-Based Capacitive Sensing Array for Normal and Shear Force Measurement. *Sensors* 10, 11 (Nov. 2010), 10211–10225. https://doi.org/10.3390/s101110211

[21] Hojung Choi, Dane Brouwer, Michael A. Lin, Kyle T. Yoshida, Carine Rognon, Benjamin Stephens-Fripp, Allison M. Okamura, and Mark R. Cutkosky. 2022. Deep Learning Classification of Touch Gestures Using Distributed Normal and Shear Force. In *2022 IEEE/RSJ International Conference on Intelligent Robots and Systems (IROS)*. 3659–3665. https://doi.org/10.1109/IROS47612.2022.9981457 ISSN: 2153-0866.

[22] Roger W. Cholewiak and Amy A. Collins. 1991. Sensory and physiological basis of touch. In *The psychology of touch*, M. Heller and W. Schiff (Eds.). Lawrence Erlbaum & Associates, Mahwah, NJ, 1–60.

[23] Eshwar Reddy Cholleti, Jonathan Stringer, Mahtab Assadian, Virginie Battmann, Chris Bowen, and Kean Aw. 2019. Highly Stretchable Capacitive Sensor with Printed Carbon Black Electrodes on Barium Titanate Elastomer Composite. *Sensors* 19, 1 (Jan. 2019), 42. https://doi.org/10.3390/s19010042 Number: 1 Publisher: Multidisciplinary Digital Publishing Institute.

[24] Steven Cramp, Cam Maccoll, and R. Bruce Wallace. 2020. Preliminary Results for Novel Shear Force Sensor using Force Sensitive Resistors. In *2020 IEEE International Instrumentation and Measurement Technology Conference (I2MTC)*. 1–6. https://doi.org/10.1109/I2MTC43012.2020.9128858 ISSN: 2642-2077.

[25] Michael T. Tolley Daniela Rus. 2015. Design, fabrication and control of soft robots. *Nature* (May 2015).

[26] Harish Devaraj, Robert Schober, Mathieu Picard, Mei Ying Teo, Cheng-Yao Lo, Wee Chen Gan, and Kean C Aw. 2019. Highly elastic and flexible multi-layered carbon black/elastomer composite based capacitive sensor arrays for soft robotics. *Measurement: Sensors* 2 (2019), 100004.

[27] Mehmet Ege Cansev, Daniel Nordheimer, Elsa Andrea Kirchner, and Philipp Beckerle. 2021. Feel-good requirements: neurophysiological and psychological design criteria of affective touch for (assistive) robots. *Frontiers in Neurorobotics* 15 (2021), 661207.

[28] Erin E. Evke, Dilara Meli, and Max Shtein. 2019. Developable Rotationally Symmetric Kirigami-Based Structures as Sensor Platforms. *Advanced Materials Technologies* 4, 12 (2019). https://doi.org/10.1002/admt.201900563

[29] Jayer Fernandes, Jiangang Chen, and Hongrui Jiang. 2021. Three-Axis Capacitive Sensor Arrays for Local and Global Shear Force Detection. *Journal of Microelectromechanical Systems* 30, 5 (2021), 799–813. https://doi.org/10.1109/JMEMS.2021.3101735

[30] Anna Flagg and Karon MacLean. 2013. Affective touch gesture recognition for a furry zoomorphic machine. In *Proceedings of the 7th International Conference on Tangible, Embedded and Embodied Interaction - TEI '13*. ACM Press, Barcelona, Spain, 25. https://doi.org/10.1145/2460625.2460629

[31] Allan Fong, Zahra Ashktorab, and Jon Froehlich. 2013. Bear-with-me: an embodied prototype to explore tangible two-way exchanges of emotional language. In *CHI '13 Extended Abstracts on Human Factors in Computing Systems on - CHI EA '13*. ACM Press, Paris, France, 1011. https://doi.org/10.1145/2468356.2468537

[32] Esther Foo, Justin Baker, Crystal Compton, and Brad Holschuh. 2020. Soft Robotic Compression Garment to Assist Novice Meditators. In *CHI Conf. on Human Factors in Comput. Syst.* ACM, Honolulu HI USA, 1–8.

[33] Yoren Gaffary, Jean-Claude Martin, and Mehdi Ammi. 2020. Haptic Expression and Perception of Spontaneous Stress. *IEEE Transactions on Affective Computing* 11, 1 (Jan. 2020), 138–150. https://doi.org/10.1109/TAFFC.2018.2830371 Conference Name: IEEE Transactions on Affective Computing.

[34] Jian Gao, Kieran Morton, Ryusuke Ishizaki, Fumiya Hamatsu, Takeshi Ohsato, and John DW Madden. 2023. Live Demonstration: Soft Flexible Capacitive Sensing Arrays for Pressure, Shear, and Proximity. In *2023 IEEE SENSORS*. 1–1. https://doi.org/10.1109/SENSORS56945.2023.10325034 ISSN: 2168-9229.

[35] Jian Gao, Zihao Pu, Ruixin Qiu, Ying Li, Xiulun Yin, Kieran Morton, Sadan Wani, Justin Wyss, Michael Steszyn, Ryusuke Ishizaki, Fumiya Hamatsu, Takeshi Ohsato, and John D.W. Madden. 2023. Smart Insole: Stand-Alone Soft 3-Axis Force Sensing Array in a Shoe. In *2023 IEEE SENSORS*. 1–4. https://doi.org/10.1109/SENSORS56945.2023.10324863 ISSN: 2168-9229.

[36] Paul Gavrikov. 2020. visualkeras. https://github.com/paulgavrikov/visualkeras.

[37] Antonia Georgopoulou and Frank Clemens. 2020. Piezoresistive Elastomer-Based Composite Strain Sensors and Their Applications. *ACS Applied Electronic Materials* 2, 7 (July 2020), 1826–1842. https://doi.org/10.1021/acsaelm.0c00278 Publisher: American Chemical Society.

[38] Abubakar Sulaiman Gezawa, Yan Zhang, Qicong Wang, and Lei Yunqi. 2020. A review on deep learning approaches for 3D data representations in retrieval and classifications. *IEEE access* 8 (2020), 57566–57593.

[39] E.B. Goldstein. 1999. *Sensation and Perception*. Wadsworth Pub. Co, Belmont, CA.

[40] Quanquan Guo, Xiaoyan Qiu, and Xinxing Zhang. 2022. Recent Advances in Electronic Skins with Multiple-Stimuli-Responsive and Self-Healing Abilities. *Materials* 15, 5 (Feb. 2022), 1661. https://doi.org/10.3390/ma15051661

[41] Xiaohui Guo, Ying Huang, Xia Cai, Caixia Liu, and Ping Liu. 2016. Capacitive wearable tactile sensor based on smart textile substrate with carbon black/silicone rubber composite dielectric. *Measurement Science and Technology* 27 (2016), 045105.

[42] Steven C. Hauser, Sarah McIntyre, Ali Israr, Håkan Olausson, and Gregory J. Gerling. 2019. Uncovering Human-to-Human Physical Interactions that Underlie Emotional and Affective Touch Communication. In *2019 IEEE World Haptics Conference (WHC)*. 407–412. https://doi.org/10.1109/WHC.2019.8816169

[43] Matthew J Hertenstein. 2002. Touch: Its communicative functions in infancy. *Human Development* 45, 2 (2002), 70–94.

[44] Sanming Hu, Zhijun Shi, Weiwei Zhao, Li Wang, and Guang Yang. 2019. Multifunctional piezoelectric elastomer composites for smart biomedical or wearable electronics. *Composites Part B: Engineering* 160 (March 2019), 595–604. https://doi.org/10.1016/j.compositesb.2018.12.077

[45] Dana Hughes, Alon Krauthammer, and Nikolaus Correll. 2017. Recognizing social touch gestures using recurrent and convolutional neural networks. In *2017 IEEE International Conference on Robotics and Automation (ICRA)*. 2315–2321. https://doi.org/10.1109/ICRA.2017.7989267

[46] Gijs Huisman. 2017. Social Touch Technology: A Survey of Haptic Technology for Social Touch. *IEEE Transactions on Haptics* 10, 3 (July 2017), 391–408. https://doi.org/10.1109/TOH.2017.2650221 Conference Name: IEEE Transactions on Haptics.

[47] Gijs Huisman, Aduén Darriba Frederiks, Betsy Van Dijk, Dirk Hevlen, and Ben Kröse. 2013. The TaSSt: Tactile sleeve for social touch. In *2013 World Haptics Conference (WHC)*. 211–216. https://doi.org/10.1109/WHC.2013.6548410

[48] Sooyeon Jeong, Cynthia Breazeal, Deirdre Logan, and Peter Weinstock. 2018. Huggable: The Impact of Embodiment on Promoting Socio-emotional Interactions for Young Pediatric Inpatients. In *Proceedings of the 2018 CHI Conference on Human Factors in Computing Systems*. ACM, Montreal QC Canada, 1–13. https://doi.org/10.1145/3173574.3174069

[49] Katsu Yamane Joohyung Kim, Alexander Alspach. 2015. 3D printed soft skin for safe human-robot interaction. *Intelligent Robots and Systems* (Dec. 2015).

[50] Annkatrin Jung, Miquel Alfaras, *et al*, and Kristina Höök. 2021. Exploring Awareness of Breathing through Deep Touch Pressure. In *CHI Conf. on Human Factors in Comput. Syst.* ACM, Yokohama Japan, 1–15.

[51] Merel M Jung, Mannes Poel, Ronald Poppe, and Dirk KJ Heylen. 2017. Automatic recognition of touch gestures in the corpus of social touch. *Journal on multimodal user interfaces* 11 (2017), 81–96.

[52] Merel M. Jung, Ronald Poppe, Mannes Poel, and Dirk K.J. Heylen. 2014. Touching the Void – Introducing CoST: Corpus of Social Touch. *Int Conf on Multimodal Interaction (ICMI)* (2014), 120–127.

[53] Da Bin Kim, Ju Han, Sun Min Sung, Min Seong Kim, Bo Kyoung Choi, Sung Jun Park, Hyae Rim Hong, Hong Je Choi, Byeong Kon Kim, Chung Hee Park, Jong Hoo Paik, Joon-Seok Lee, and Yong Soo Cho. 2022. Weave-pattern-dependent fabric piezoelectric pressure sensors based on polyvinylidene fluoride nanofibers electrospun with 50 nozzles. *npj Flexible Electronics* 6, 1 (Aug. 2022), 1–9. https://doi.org/10.1038/s41528-022-00203-6 Number: 1 Publisher: Nature Publishing Group.

[54] Hyeohn Kim, Gwangmook Kim, Taehoon Kim, Sangwoo Lee, Donyoung Kang, Min-Soo Hwang, Youngcheol Chae, Shinill Kang, Hyungsuk Lee, Hong-Gyu Park, and Wooyoung Shim. 2018. Transparent, Flexible, Conformal Capacitive Pressure Sensors with Nanoparticles. *Small* 14, 8 (2018), 1703432. https://doi.org/10.1002/smll.201703432 _eprint: https://onlinelibrary.wiley.com/doi/pdf/10.1002/smll.201703432.

[55] Young-Min Kim, Seong-Yong Koo, Jong Gwan Lim, and Dong-Soo Kwon. 2010. A robust online touch pattern recognition for dynamic human-robot interaction. *IEEE Transactions on Consumer Electronics* 56, 3 (2010), 1979–1987.

[56] James H. Kryklywy, Preeti Vyas, Karon E. MacLean, and Rebecca M. Todd. 2023. Characterizing affiliative touch in humans and its role in advancing haptic design. *Annals of the New York Academy of Sciences* 1528, 1 (2023), 29–41. https://doi.org/10.1111/nyas.15056

[57] Benjamin Lemke, Marc Baumann, Pascal Gieschke, Rajashree Baskaran, and Oliver Paul. 2013. Piezoresistive CMOS-compatible sensor for out-of-plane shear stress. *Sensors and Actuators A: Physical* 189 (2013), 488–495. https://doi.org/10.1016/j.sna.2012.10.014

[58] Li-Wei Lo, Hongyang Shi, Haochuan Wan, Zhihao Xu, Xiaobo Tan, and Chuan Wang. 2020. Inkjet-printed soft resistive pressure sensor patch for wearable electronics applications. *Advanced Materials Technologies* 5, 1 (2020), 1900717.

[59] Francis McGlone, Johan Wessberg, and Håkan Olausson. 2014. Discriminative and Affective Touch: Sensing and Feeling. *Neuron* 82, 4 (May 2014), 737–755. https://doi.org/10.1016/j.neuron.2014.05.001

[60] India Morrison, Line S. Löken, and Håkan Olausson. 2010. The skin as a social organ. *Experimental Brain Research* 204, 3 (July 2010), 305–314. https://doi.org/10.1007/s00221-009-2007-y

[61] Kieran Morton, Ryusuke Ishizaki, Zi Chen, Mirza S. Sarwar, and John D. W. Madden. 2023. Soft Three-Axis Capacitive Force Sensor for Robotic E-Skin on Curved Surfaces. *IEEE Sensors Letters* 7, 10 (2023), 1–4. https://doi.org/10.1109/LSENS.2023.3303082

[62] Shunsuke Nagahama, Kayo Migita, and Shigeki Sugano. 2019. Soft Magnetic Powdery Sensor for Tactile Sensing. *Sensors (Basel, Switzerland)* 19, 12 (June 2019), 2677. https://doi.org/10.3390/s19122677

[63] E Nagy. 2011. Sharing the moment: the duration of embraces in humans. *Journal of Ethology* 29 (2011), 389–393. https://doi.org/10.1007/s10164-010-0260-y

[64] Ngoc Tan Nguyen, Mirza Saquib Sarwar, Claire Preston, Aziliz Le Goff, Cedric Plesse, Frederic Vidal, Eric Cattan, and John DW Madden. 2019. Transparent stretchable capacitive touch sensor grid using ionic liquid electrodes. *Extreme Mechanics Letters* 33 (2019), 100574.

[65] Baoqing Nie, Ruya Li, Jennifer Cao, James Brandt, and Tingrui Pan. 2015. Flexible Transparent Iontronic Film for Interfacial Capacitive Pressure Sensing. *Advanced Materials Technologies* 27, 39 (2015), 6055–6062.

[66] Aditya Shekhar Nittala, Anusha Withana, Narjes Pourjafarian, and Jürgen Steimle. 2018. Multi-Touch Skin: A Thin and Flexible Multi-Touch Sensor for On-Skin Input. In *Proceedings of the 2018 CHI Conference on Human Factors in Computing Systems - CHI '18*. ACM Press, 1–12. https://doi.org/10.1145/3173574.3173607 event-place: Montreal QC, Canada.

[67] Masa Ogata, Yuta Sugiura, Yasutoshi Makino, Masahiko Inami, and Michita Imai. 2013. SenSkin: adapting skin as a soft interface. In *Proceedings of the 26th Annual ACM Symposium on User Interface Software and Technology* (St. Andrews, Scotland, United Kingdom) *(UIST '13)*. Association for Computing Machinery, New York, NY, USA, 539–544. https://doi.org/10.1145/2501988.2502039

[68] Jonghwa Park, Youngoh Lee, Jaehyung Hong, Youngsu Lee, Minjeong Ha, Youngdo Jung, Hyuneui Lim, Sung Youb Kim, and Hyunhyub Ko. 2014. Tactile-direction-sensitive and stretchable electronic skins based on human-skin-inspired interlocked microstructures. *ACS nano* 8, 12 (2014), 12020–12029.

[69] Patrick Parzer, Florian Perteneder, Kathrin Probst, Christian Rendl, Joanne Leong, Sarah Schuetz, Anita Vogl, Reinhard Schwoediauer, Martin Kaltenbrunner, Siegfried Bauer, and Michael Haller. 2018. RESi: A Highly Flexible, Pressure-Sensitive, Imperceptible Textile Interface Based on Resistive Yarns. In *Proceedings of the 31st Annual ACM Symposium on User Interface Software and Technology* (, Berlin, Germany,) *(UIST '18)*. Association for Computing Machinery, New York, NY, USA, 745–756. https://doi.org/10.1145/3242587.3242664

[70] Brijesh Prasad, Fateh Singh Gill, and Varij Panwar. 2020. Piezoresistive strain sensing behavior of flexible conductive microporous membrane using acidic ionic liquid. *Journal of Molecular Liquids* 319 (Dec. 2020), 114309. https://doi.org/10.1016/j.molliq.2020.114309

[71] J. Qin et al. 2021. Flexible and Stretchable Capacitive Sensors with Different Microstructures. *Advanced Materials* 33, 34 (2021), 2008267. https://doi.org/10.1002/adma.202008267

[72] Mirza Saquib Sarwar, Yuta Dobashi, Claire Preston, Justin K. M. Wyss, Shahriar Mirabbasi, and John David Wyndham Madden. 2017. Bend, stretch, and touch: Locating a finger on an actively deformed transparent sensor array. *Science Advances* 3, 3 (March 2017), e1602200. https://doi.org/10.1126/sciadv.1602200

[73] Mirza S. Sarwar, Ryusuke Ishizaki, Kieran Morton, Claire Preston, Tan Nguyen, Xu Fan, Bertille Dupont, Leanna Hogarth, Takahide Yoshiike, Ruixin Qiu, Yiting Wu, Shahriar Mirabbasi, and John D.W. Madden. 2023. Touch, press and stroke: a soft capacitive sensor skin. *Scientific Reports* 13 (2023). https://doi.org/10.1038/s41598-023-43714-6

[74] Mirza S. Sarwar and Katsu Yamane. 2021. Large-Area Conformable Sensor for Proximity, Light Touch, and Pressure-Based Gesture Recognition. In *2021 IEEE/RSJ International Conference on Intelligent Robots and Systems (IROS)*. https://doi.org/10.1109/iros51168.2021.9635943

[75] Mirza Saquib us Sarwar. 2019. *Soft capacitive sensors for proximity, touch, pressure and shear measurements*. PhD Thesis. University of British Columbia. https://doi.org/10.14288/1.0378695 Series: Electronic Theses and Dissertations (ETDs) 2008+.

[76] Skipper Seabold and Josef Perktold. 2010. statsmodels: Econometric and statistical modeling with python. In *9th Python in Science Conference*.

[77] Sudeep Sharma, Ashok Chhetry, Md Sharifuzzaman, Hyosang Yoon, and Jae Yeong Park. 2020. Wearable Capacitive Pressure Sensor Based on MXene Composite Nanofibrous Scaffolds for Reliable Human Physiological Signal Acquisition. *ACS Applied Materials & Interfaces* (April 2020). https://doi.org/10.1021/acsami.0c05819

[78] Ahmed W. Shehata, Mayank Rehani, Zaheera E. Jassat, and Jacqueline S. Hebert. 2020. Mechanotactile Sensory Feedback Improves Embodiment of a Prosthetic Hand during Active Use. *Frontiers in Neuroscience* (March 2020). https://doi.org/10.3389/fnins.2020/00263

[79] Christopher G. Atkeson Siddharth Sanan, Michael H. Ornstein. 2011. Physical human interaction for an inflatable manipulator. *International Conference of the IEEE Engineering in Medicine and Biology Society* (Dec. 2011).

[80] David Silvera Tawil, David Rye, and Mari Velonaki. 2012. Interpretation of the modality of touch on an artificial arm covered with an EIT-based sensitive skin. *The International Journal of Robotics Research* 31, 13 (2012), 1627–1641.

[81] David Silvera-Tawil, David Rye, and Mari Velonaki. 2014. Artificial skin and tactile sensing for socially interactive robots: A review. *Robotics and Autonomous Systems* (Sept 2014). https://doi.org/10.1016/j.robot.2014.09.009

[82] David Sun, Pablo Paredes, and John Canny. 2014. MouStress: detecting stress from mouse motion. In *Proceedings of the SIGCHI Conference on Human Factors in Computing Systems*. ACM, Toronto Ontario Canada, 61–70. https://doi.org/10.1145/2556288.2557243

[83] Marc Teyssier, Gilles Bailly, Catherine Pelachaud, and Eric Lecolinet. 2020. Conveying Emotions Through Device-Initiated Touch. *IEEE Transactions on Affective Computing* (2020), 1–1. https://doi.org/10.1109/TAFFC.2020.3008693 Conference Name: IEEE Transactions on Affective Computing.

[84] Marc Teyssier, Gilles Bailly, Catherine Pelachaud, Eric Lecolinet, Andrew Conn, and Anne Roudaut. 2019. Skin-On Interfaces: A Bio-Driven Approach for Artificial Skin Design to Cover Interactive Devices. In *Proceedings of the 32nd Annual ACM Symposium on User Interface Software and Technology*. ACM, New Orleans LA USA, 307–322. https://doi.org/10.1145/3332165.3347943

[85] Marc Teyssier, Gilles Bailly, Catherine Pelachaud, Eric Lecolinet, Andrew Conn, and Anne Roudaut. 2019. Skin-On Interfaces: A Bio-Driven Approach for Artificial Skin Design to Cover Interactive Devices. In *Proceedings of the 32nd Annual ACM Symposium on User Interface Software and Technology* (New Orleans, LA, USA) *(UIST '19)*. Association for Computing Machinery, New York, NY, USA, 307–322. https://doi.org/10.1145/3332165.3347943

[86] Marc Teyssier, Brice Parilusyan, Anne Roudaut, and Jürgen Steimle. 2021. Human-Like Artificial Skin Sensor for Physical Human-Robot Interaction. In *2021 IEEE International Conference on Robotics and Automation (ICRA)*. 3626–3633. https://doi.org/10.1109/ICRA48506.2021.9561152

[87] Tito Pradhono Tomo, Massimo Regoli, Alexander Schmitz, Lorenzo Natale, Harris Kristanto, Sophon Somlor, Lorenzo Jamone, Giorgio Metta, and Shigeki Sugano. 2018. A New Silicone Structure for uSkin—A Soft, Distributed, Digital 3-Axis Skin Sensor and Its Integration on the Humanoid Robot iCub. *IEEE Robotics and Automation Letters* 3, 3 (2018), 2584–2591. https://doi.org/10.1109/LRA.2018.2812915

[88] Vasiliki Tsaknaki, Kelsey Cotton, Pavel Karpashevich, and Pedro Sanches. 2021. "Feeling the Sensor Feeling you": A Soma Design Exploration on Sensing Non-habitual Breathing. In *Proceedings of the 2021 CHI Conference on Human Factors in Computing Systems*. ACM, Yokohama Japan, 1–16. https://doi.org/10.1145/3411764.3445628

[89] Torben Wallbaum, Janko Timmermann, Wilko Heuten, and Susanne Boll. 2015. Forget Me Not: Connecting Palliative Patients and Their Loved Ones. In *Proceedings of the 33rd Annual ACM Conference Extended Abstracts on Human Factors in Computing Systems*. ACM, Seoul Republic of Korea, 1403–1408. https://doi.org/10.1145/2702613.2732772

[90] Rongrong Wang, Francis Quek, Deborah Tatar, Keng Soon Teh, and Adrian Cheok. 2012. Keep in touch: channel, expectation and experience. In *Proceedings of the SIGCHI Conference on Human Factors in Computing Systems*. ACM, Austin Texas USA, 139–148. https://doi.org/10.1145/2207676.2207697

[91] Shihang Wang, Yancheng Wang, Zhijian Chen, and Deqing Mei. 2022. Kirigami Design of Flexible and Conformable Tactile Sensor on Sphere-shaped Surface for Contact Force Sensing. *Advanced Materials Technologies* 8, 3 (2022). https://doi.org/10.1002/admt.202200993

[92] Ning Wei, Yan Li, Chunqin Zhu, and Yuxi Tang. 2022. Highly Compressible Elastic Aerogel Spring-Based Piezoionic Self-Powering Pressure Sensor for Multifunctional Wearable Electronics. *Nanomaterials* 12, 15 (2022), 2574.

[93] Jacob O Wobbrock, Leah Findlater, Darren Gergle, and James J Higgins. 2011. The aligned rank transform for nonparametric factorial analyses using only anova procedures. In *Proceedings of the SIGCHI conference on human factors in computing systems*. 143–146.

[94] Justin Kian Ming Wyss. 2020. *A soft flexible and stretchable pressure sensor array designed to warn of pressure ulcer formation*. Ph. D. Dissertation. University of British Columbia. https://doi.org/10.14288/1.0394049

[95] Kai Xing, Zhen Ding, Shuai Jiang, Xueyan Ma, Kai Yang, Chifu Yang, Xiang Li, and Feng Jiang. 2018. Hand gesture recognition based on deep learning method. In *2018 IEEE Third International Conference on Data Science in Cyberspace (DSC)*. IEEE, 542–546.

[96] Xiulun Yin, Ziqiang Chen, Nima Bakhshi, Oliver Tong, Xiaoxiao Xiong, Yizhong Chen, Ying Li, Jian Gao, Mirza Saquib Sarwar, Anoush Poursartip, and John DW Madden. 2023. Smart Roller: Soft Sensor Array for Automated Fiber Placement. *Advanced Sensor Research* (Aug 2023). https://doi.org/10.1002/adsr.202200074

[97] Steve Yohanan and Karon E. MacLean. 2012. The Role of Affective Touch in Human-Robot Interaction: Human Intent and Expectations in Touching the Haptic Creature. *International Journal of Social Robotics* 4, 2 (April 2012), 163–180. https://doi.org/10.1007/s12369-011-0126-7

[98] Nan Zhou and Jun Du. 2016. Recognition of social touch gestures using 3D convolutional neural networks. In *Pattern Recognition: 7th Chinese Conference, CCPR 2016, Chengdu, China, November 5-7, 2016, Proceedings, Part I 7*. Springer, 164–173.

[99] Mengjia Zhu, Amirhossein H. Memar, Aakar Gupta, Majed Samad, Priyanshu Agarwal, Yon Visell, Sean J. Keller, and Nicholas Colonnese. 2020. PneuSleeve: In-fabric Multimodal Actuation and Sensing in a Soft, Compact, and Expressive Haptic Sleeve. In *Proceedings of the 2020 CHI Conference on Human Factors in Computing Systems*. ACM, Honolulu HI USA, 1–12. https://doi.org/10.1145/3313831.3376333

A SUPPLEMENT: DETAILED DESIGN CONSIDERATIONS

A.1 Decoupling Shear and Normal Stress

Validation of this technology requires establishing that we are indeed measuring shear and normal stresses as separate constructs. These quantities are necessarily linked: a minimum normal stress must be exerted to engage shear (by an amount dependent on sliding *vs.* static mode and mutual friction). However, we should be able to detect normal stress with zero shear, and shear across a range of normal stresses. §5.2 and previous characterization [73] show that the forces can largely be separated. We discuss how this occurs, and where it is at risk.

Ideal behavior and non-ideal effects: Differential 3-dimensional deflections of the five pillars in each taxel result in channel capacitance changes, which are variously combined to estimate normal and shear components. Several factors can potentially interfere, including cross-talk from mechanical coupling within and between taxels and electrical coupling between electrodes.

Most significantly for this sensor geometry, stress computations assume uniform cross-taxel stress. In fact, for a sub-taxel-size indenter, linearity drops away from the taxel center, minimized in the inter-taxel zone; and if normal stress is localized to one of the four outer electrodes, it mistakenly appears as shear. We largely address this by computing virtual taxels (§4.1.5).

Surface friction interaction with sensitivity: The sensor's cover layer had to (among other criteria) provide a finger-fabric mutual friction that activated shear without being too sticky to slide. As we increased normal-shear sensitivity with each prototype, we had to increase surface friction coefficient to continue to activate shear at lower normal forces. At the same time, one of our sensitivity-increasing strategies (lowering the shore-hardness of the elastomer - see below) made the surface more soft and tacky. While the bare surface was too tacky to slide on, adding carefully chosen fabric as a surface layer optimized mutual friction while protecting the structure.

Data collection: To validate sensitivity and cross-axis independence, we curated a gesture set with diversity in activation of shear and normal stresses (§6.1.1), then confirmed this diversity by examining model feature involvement by gesture. In the future, we need more definitive validation with gestures that represent experienced emotion and minimal control, while we examinat saturation and activation to ensure sensor range.

A.2 Minimizing the Normal Stress Detection Threshold

While early sensor versions indicated normal-stress readings for affective gestures which seemed reasonable, we found that even after amplification, autoscaling, and other signal processing, our ML models worked better when participants were asked to use "heavy" gestures. We substantively reduced detection threshold by several means. In later collections we instructed participants to use a "natural" weight, and report accuracy for this data.

Sensor design: The two most effective sensitivity adjustments were generally to reduce taxels' vertical (z-axis) structural stiffness. First, we switched from rectangular to pyramidal pillars, which were more compressible over same deflection and thus amplified capacitance output. We note this as another tradeoff: we had earlier found that rectangular pillars had lower stress sensitivity levels, but also that they may have better cross-taxel mechanical consistency.

Secondly, we reduced the elastomer's shore hardness. As a tradeoff, this softer material was more fragile, and more tacky to the touch.

We addressed both of these issues with a surface covering, which on the positive side now adhered easily to the Ecoflex and the choice of which allowed us to control surface friction independent of elastomer material.

Tradeoffs in using soft material to lower threshold: A major design change of softening the elastomer to increase mechanical response came with drawbacks. The first is increased viscoelasticity. The current prototype requires seconds for full relaxation from a heavy sustained deformation, with possible drift in the capacitance response (Figure 11).

This introduces error in a direct capacitance-stress conversion, particularly for light deflection immediately after a large one. Although we attained good gesture classification, it would doubtless improve, *e.g.*, by combining stiffer materials with more sensitive electronics. Meanwhile, viscoelastic modeling could correct the response.

Capacitance saturation (with high stress that fully compresses the pillars) dropped; this is possibly addressable by increasing sensor thickness, but with its own consequence (below). The tacky surface inhibits sliding contact (addressable with a suitably slick fabric top-layer); and there were durability effects (§**??**).

Further possible improvement: Capacitance changes are determined by geometry, *i.e.*, proportional to inter-electrode separation. When force is applied, the strain is inversely proportional to the effective elastic modulus (intrinsic stiffness resulting from material modulus and pillar structure). However, reduction in elastic modulus is generally associated with higher loss, greater stress relaxation and lower strength, so these effects must be balanced. Electronics are also a key part in sensor improvement, as factors such as the signal noise magnitude strongly affect minimum resolvable stress for the sensor. Improvements to signal quality are possible through filters or a higher number of collected samples per measurement, but these tend to lower the overall measurement rate.

A.3 Sensor Size, Resolution and Scaling

The taxel size, array layout, and density we report on were influenced by ease of fabrication, and the spatial resolution which has proven successful in the past at affective-touch gesture recognition for past normal-stress array sensors. While we did not alter these physical properties in the iterations leading to the reported prototype, the *ability* to do so could be a benefit of the technology. We consider the tradeoffs.

Smaller taxels: Reducing taxel width requires concomitant thickness reduction. The thinner surface layer could feel stiffer, reduce saturation stress; and fabrication will require more precision.

Increasing resolution with virtual taxels: We analytically leveraged our taxels' multi-channel structure to improve and smooth spatial

resolution. This nearly 2x data augmentation step utilized information only from contacted capacitance channels. They yielded better localization of between-taxel contact when compared with either taking the average normal/shear stress readings between adjacent taxels or simply repeating taxel readings in column and row directions of the sensing array. With the same 3DCNN model tweaked for these two methods, we saw higher overall classification accuracy for both all-inclusive and leave-one-out experiments.

Sloped pillars for easier demolding: Demolding represents a critical obstacle to component miniaturaztion, particularly as softer, stickier elastomers were used. The pyramidal pillars which we used to improve stress sensitivity also facilitated release of the highly viscous Ecoflex from molds during fabrication, allowing us to create smaller taxels. We would expect a similar result from any non-rectangular pillar structure.

Towards smaller arrays with minimal modification: We chose this array technology in part due to its adaptability. In the elastomer-FPCB sensing stack, the conductive fabric T_x connections are oriented parallel to the FPC connection, perpendicular to the FPCB-embedded R_x tracks. Hence, the sensing array can literally be cut *down* into any array format smaller than the 6×6 layout and perform normal/shear stress sensing for the remaining taxels without modifying the microcontroller firmware.

Towards larger arrays through linking: To achieve larger coverage, specific to the PSoC chip we used, up to 4 sets of microcontroller-sensor systems can be implemented at once with an external BLE controller gathering the data concurrently from those 4 microcontrollers. If more than four 6×6 sensing arrays are needed, data transmission can be reverted to hard-wired with reserved Inter-Integrated Circuit (I2C) connections on the microcontroller.

A.4 Multi-Axis Flexibility

For our application space, we are interested in curved surfaces, incorporation into flexible structures and testing in environments where feedback from affective touch is sought. This sensor's base is a conventional polyamide-based flexible PCB, allowing significant bending on a single axis – it cannot currently wrap over complex surfaces.

Multi-axis curvature will be possible by eliminating the PCB altogether [72]; or by introducing "kirigami" cuts into the PCB to allow nonuniform shape conformation [28, 91]. These accommodations for complex underlying curvatures would require careful reconsideration of the electrode placement and alignment for the sensor, such as simplifying traces or reducing overall design complexity.

Initial characterizatino with this technology approach suggests that sensitivity becomes dependent on curvature when the radius of curvature becomes smaller than the taxel width [61], motivating smaller taxels and higher spatial resolution.

A.5 Robustness

We saw signs of damage over the 26.5 hours our primary test sensor was used. For their intended use in protracted and less-monitored contexts, robustness can be improving through bonding, and adjusting the tradeoff between sensitivity, structure and materials — where recent improvements in fast, high-dynamic-range electronics may provide another path attaining high sensitivity with higher-stiffness materials (§**??**).

A.6 Pipeline and Modeling

Towards continuous sampling: While we eventually plan for continuous, realtime processing of live data, at this development stage it was necessary to collect data in delineated samples (data instances from discrete trials), and isolate preprocessing from collection so we could explore modeling approaches. This sets us up in the future to more effectively optimize for sufficient computational speed to keep up with live collection.

Model improvement and explainability: We found that a 3DCNN model identified predictions most quickly, but we relied on manual feature engineering for insight. We speculate that classical models may be more effective with data instances longer than our current 2s windows. Classical models often rely on well-understood statistical relationships. With a longer data window, these assumptions become more reliable. Deep learning models, on the other hand, need to learn these relationships from the data itself, which can be less efficient with longer windows. We also imagine that a deep learning model able to target more information in the time domain, *e.g.*, ConvLSTM or transformer-based models, will outperform 3DCNN.

A.7 Debugging

Complex pipeline hampered debugging: This project had a complex data pipeline. A number of human individuals (exhibiting normal, *i.e.*, substantial, population variance) are instructed to touch the sensor with a specified protocol which they follow imperfectly. A sensor (with an electromechanical structure that might be degrading at an unknown rate) is deflected, a capacitance read and filtered. A signal is transmitted through wires and air, received, conditioned and modeled in various ways.

We had to develop and test the full pipeline all together. We typically discovered an issue's existence only when the final stage delivered lower-than-expected classification accuracy. It was difficult to insert intermediate checkpoints, being often unclear what to look for, or how much. For example, our early prototypes seemed to be delivering healthy normal-stress data, yet modeling lagged results from other technology. We had been forced to use different ML models by nature of the data; so, was the problem model, noise, preprocessing, or the data itself? In the end it was a combination of stress *thresholds* plus modeling bugs. In other words, when recognition *accuracy* was weak, the pipeline meant multiple data-collection iterations to identify *thresholds* as the culprit.

Sensor wellness checks and built-in monitoring points throughout pipeline: We eventually found ways to build in monitoring, *e.g.*, fast instrumented taxel re-characterization.

We instituted and iteratively improved within-study sensor 'wellness checks', conducted between participants and between data-collection-series, to keep track of degradation and faulty data. For example, a check might involve placing a known weight on 5 different locations on the sensor to check that readings are satisfactory.

Finally, we refined an efficient gesture collection protocol, together with a quickly accessible participant pool, so that we could do new collections in a minimal amount of time.

In future, we plan to add a 3-axis stress plate under the gesture collection setup as a reliable ground-truth sensor check, and automate all-taxel characterization by programming a 3D printer extruder with controlled motion sequences.

A.8 Practicality

In §5.3, we reported on one prototype's degradation after an estimated 26.5 hours of use. While our present stage of development is about feasibility and verifying that we have a platform suitable for studying the role of shear in affective touch, this initial level of durability combined with the low cost of fabrication (<5 USD for the 6×6 sensing array) suggests the technology is already suitable for monitored laboratory research with checks in place to replace or repair as issues arise.

B SUPPLEMENT: CAPACITANCE CALCULATION FROM RAWCOUNT BY OUR PSOC-BASED CUSTOM MICROCONTROLLER

See Supplemental Materials for:

- **Figure B.1:** *CAPSENSE^{TM} mutual capacitance (CSX) sensing configuration, copyright Cypress Semiconductor 2023.*
- **Figure B.2:** *: CAPSENSE^{TM} mutual capacitance (CSX) sensing principle*

C SUPPLEMENT: IMPLEMENTATION OF VIRTUAL TAXELS

See Supplemental Materials for:

- **Figure C.1:** *Shear sensing array response while pressing at the a) center, b) edge, c) corner of a taxel.*

D SUPPLEMENT: GESTURAL DATA AND CHARACTERIZATION

See Supplemental Materials for:

- **Figure D.1:** *Gesture execution and heatmap on a flat surface on Sensor A (no fabric covering).*
- **Figure D.2:** *Gesture execution and heatmap on a curved-surface, Sensor B (with fabric covering).*
- **Figure D.3:** *Normal stress profile for 16 participants while performing 9 different gestures (sorted by median).*
- **Figure D.4:** *Confusion matrices for the 16 leave-one-out models tests with 5-round median accuracies.*

E SUPPLEMENT: CHARACTERIZATION RESULTS

See Supplemental Materials for:

- **Figure E.1:** *The Normal Stress response of a taxel of previous version of the sensor*
- **Table E.1:** *Normal performance of a taxel using different material and microstructure*
- **Figure E.2 & E.;3** *: The left figure is normal stress characterization data loading portion to the maximum displacement; The right figure is shear X-axis characterization data loading part to the maximum displacement. The speed is constant at 2mm/s.*
- **Figure E.4:** $\Delta C/C0$ *versus Normal Stress*
- **Figure E.5:** *Force vsersus* $\Delta C/C0$
- **Table E.2:** *Performance of four characterized taxels with an average shear sensitivity of 0.013/kPa*
- **Figure E.6:** *The normal stress response of the taxel being characterized and its adjacent taxels.*
- **Figure E.7:** *The shear stress response of the taxel being characterized and its adjacent taxels.*
- **Figure E.8:** *Sensor Characterization Setup for Curve Surface. a) THORLABS 3-axis NanoMaxTM Flexure stage equipped with an ATI Multi-axis Force/Torque (F/T) load cell. b) Curved Ridges mounted on the base of the characterization setup. c) Close-up view of a taxel on the curved surface undergoing characterization.*
- **Figure E.9:** *The shear stress response of a taxel characterized on a flat surface.*
- **Figure E.10:** *The shear stress response of the taxels characterized on an 80mm radius surface.*
- **Figure E.11:** *The shear stress response of the taxels characterized on a 30mm radius surface*
- **Table E.3:** *Performance of a taxel on the flat and curved surface.*
- **Figure E.12:** *The shear stress response of a corner taxel near the connector.*